



Master's thesis
Astrophysical Sciences

Ion Reflection at the Earth's Quasi-Perpendicular Bow Shock in Vlasiator

Antti Kukkola

February 14, 2023

Supervisor(s): Dr. Andreas Johlander

Censor(s): prof. Minna Palmroth
 Dr. Markus Battarbee

UNIVERSITY OF HELSINKI
MASTER'S PROGRAMME IN PARTICLE PHYSICS AND ASTROPHYSICAL SCIENCES

P.O. Box 64 (Gustaf Hällströmin katu 2)
FI-00014 University of Helsinki

Tiedekunta — Fakultet — Faculty		Koulutusohjelma — Utbildningsprogram — Education programme	
Faculty of Science		Master's Programme in Particle Physics and Astrophysical Sciences	
Tekijä — Författare — Author			
Antti Kukkola			
Työn nimi — Arbetets titel — Title			
Ion Reflection at the Earth's Quasi-Perpendicular Bow Shock in Vlasiator			
Opintosuunta — Studieriktning — Study track			
Astrophysical Sciences			
Työn laji — Arbetets art — Level		Aika — Datum — Month and year	Sivumäärä — Sidoantal — Number of pages
Master's thesis		February 14, 2023	56 pages
Tiivistelmä — Referat — Abstract			
<p>A stream of charged particles known as the solar wind constantly flows with supersonic speed in our solar system. As the supersonic solar wind encounters Earth's magnetic field, a bow shock forms where the solar wind is compressed, heated and slowed down. Not all ions of the solar wind pass through the shock but rather a portion are reflected back upstream. What happens to the reflected ions depends on the magnetic field geometry of the shock. In the case where the angle between the upstream magnetic field and the shock normal vector is small, the reflected ions follow the magnetic field lines upstream and form a foreshock region. In this case the shock is called quasi-parallel. In the case of a quasi-perpendicular shock, where the angle is large, the reflected ions gyrate back to the shock, accelerated by the convection electric field. Upon returning to the shock, the ions have more energy and either pass through the shock or are reflected again, repeating the process. Ion reflection is important for accelerating ions in shocks. In this work we study the properties and ion reflection of the quasi-perpendicular bow shock in Vlasiator simulations.</p> <p>Vlasiator is a plasma simulation which models the interaction between solar wind and the Earth's magnetic field. The code simulates the dynamics of plasma using a hybrid-Vlasov model, where ions are represented as velocity distribution functions (VDF) and electrons as magnetohydrodynamic fluid. Two Vlasiator runs are used in this work. The ion reflection is studied by analysing VDFs at various points in the quasi-perpendicular shock. The analysis is performed with reflections in multiple different frames.</p> <p>A virtual spacecraft is placed in the simulation to study shock properties and ion dynamics, such as the shock potential and ion reflection efficiency. These are compared to spacecraft observations and other simulations to test how well Vlasiator models the quasi-perpendicular bow shock.</p> <p>We find that the ion reflection follows a model for specular reflection well in all tested frames, especially in the plane perpendicular to the magnetic field. In addition, the study was extended to model second specular reflections which were also observed. We conclude that the ions in Vlasiator simulations are nearly specularly reflected.</p> <p>The properties of the quasi-perpendicular bow shock are found to be in quantitative agreement with spacecraft observations. Ion reflection efficiency is found to match observations well. Shock potential investigations revealed that spacecraft observations may have large uncertainties compared to the real shock potential.</p>			
Avainsanat — Nyckelord — Keywords			
Bow shock, Vlasiator, particle acceleration, ion reflection, space physics			
Säilytyspaikka — Förvaringsställe — Where deposited			
Muita tietoja — övriga uppgifter — Additional information			

Contents

1	Introduction	1
1.1	Plasmas	1
1.2	Shocks	2
1.3	Ion reflection	4
1.4	Earth’s bow shock	7
2	Vlasiator	11
2.1	Simulation model	11
2.2	Simulation runs used	14
2.3	This work	16
3	Reflected ion populations	17
3.1	Specular reflection	17
3.1.1	Reflected ion velocities	17
3.1.2	Transformation to the simulation frame	20
3.1.3	Estimating specular reflection	21
3.2	Determination of the shock normal vector	23
3.3	Beyond specular reflection	25
3.3.1	Reflection in other frames	25
3.3.2	Two reflections	31
3.4	Traversing the shock, analysis of one quasi-perpendicular shock cross- ing	37
4	Structure of the quasi-perpendicular bow shock	43
4.1	Bow shock cross section	43
4.2	Virtual spacecraft	44
4.3	Shock potential	46
4.4	Ion dynamics at the shock	49

5	Discussion and conclusions	53
	Acknowledgements	56
	Bibliography	56

1. Introduction

1.1 Plasmas

A stream of charged particles, which originates from the Sun, constantly flows in our solar system. This stream is a plasma which is a state of matter formed from neutral atoms when high-energy collisions or ionizing radiation strips away the electrons of the atoms. Plasma typically consists of positive ions and negative electrons. The number of positive and negative charges in plasma cancel out on large scales, making it globally neutral. This is called quasineutrality. Even small charge imbalances cause rapid flow of electrons to re-establish the neutrality. A distinctive feature of plasma is that its behaviour is largely affected by electric and magnetic forces compared to just mechanical collisions in neutral gases. In some plasmas, the mean free path between collisions is much larger than the system itself making the plasma collisionless. In collisionless plasmas the motion of the particles is determined by electromagnetic fields.

A characteristic length scale for a plasma is the decay scale of the electric potential known as the Debye length

$$\lambda_D = \sqrt{\frac{\epsilon_0 k_B T_e}{n e^2}}, \quad (1.1)$$

where ϵ_0 is the permittivity of free space, k_B is the Boltzmann constant, n is the number density, e is the charge of an electron and T_e is the electron temperature. The plasma shields the particle so its potential ϕ is weakened exponentially with distance r according to

$$\phi = \phi_0 \exp(-r/\lambda_D). \quad (1.2)$$

The Debye length is the length in which particles screen out potentials. Beyond the Debye length no significant charge separation can occur. Using the Debye length we can get another definition for a plasma: The system size L has to be significantly larger than the Debye length $L \gg \lambda_D$ for the screening to happen.

Not only is plasma found in our Solar system but also just about everywhere in the Universe for example in stars and interstellar space. Here on Earth we can see plasma in lightnings and auroras. Still, plasma is relatively rare on Earth which is why it may surprise that plasma is the most abundant visible matter in the Universe. Plasmas in astrophysical settings are often collisionless.

The stream of particles flowing in our solar system is called the solar wind. It is a plasma released from the upper part of the atmosphere of the Sun, called the corona. The solar wind, consisting mainly of electrons, protons and alpha particles [Geiss et al., 1995], carries a magnetic field which is frozen-in to the plasma. This means the magnetic field is restricted to move with the plasma. The magnetic field in the solar wind is called the interplanetary magnetic field (IMF). The solar wind, along with the magnetic field lines, flow radially outwards from the Sun's surface but are twisted into a spiral shape as the origins of the flow rotate with the Sun's surface. This is known as the Parker spiral [Parker, 1958]. The shape of the spiral is somewhat distorted as velocity of the solar wind varies due to solar activity.

1.2 Shocks

When an obstacle moves relative to a medium with a speed faster than the wave carrying information in the medium, a shock forms in front of the obstacle. Shock waves are transitions between a supersonic flow and a subsonic flow with an abrupt change in the pressure of the material. A shock can either form if the obstacle is moving with supersonic speeds or if the flow is hitting the obstacle with supersonic speeds. A common example of a shock are supersonic aircrafts that move seemingly silently until the shock arrives after the aircraft.

Shocks are common in plasmas in the universe. In collisionless plasmas the shock is also collisionless. This means the length scale of the shock is much shorter than the collisional mean free path of the particles in the plasma. In collisionless shocks, energy is carried by the wave-particle interaction caused by electromagnetic fields. A variety of different wave modes can be present in plasma.

An important tool in describing shocks is the Mach number $M = V/c_s$, where V is the relative velocity of the obstacle to the bulk flow and c_s is the speed of sound in the medium. A shock forms when $M > 1$. For collisionless plasmas the conditions are different and c_s has to be replaced by a more relevant speed. It is common in plasma physics to replace this with the speed of an Alfvén wave called

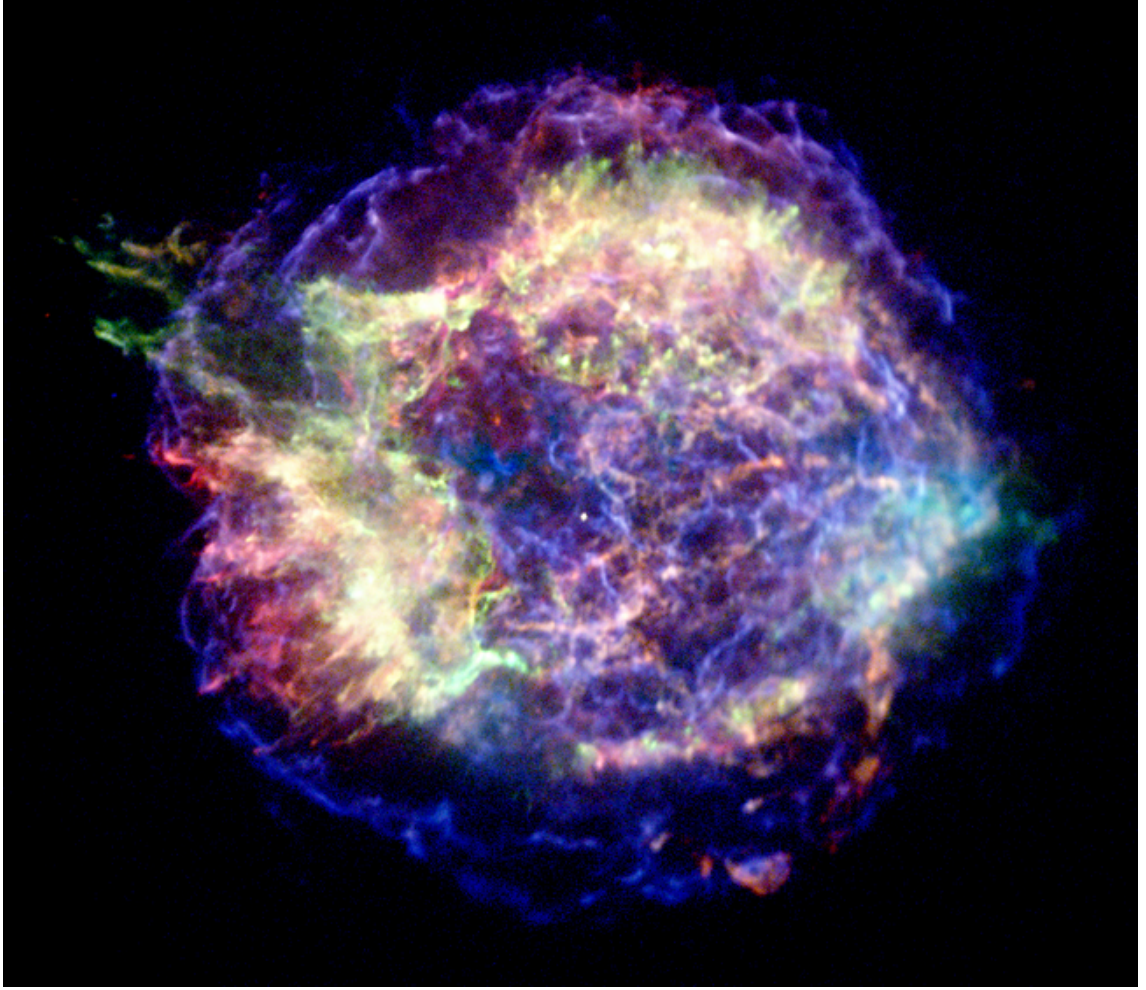


Figure 1.1: Supernova remnant Cassiopeia A imaged by Chandra in X-rays. A shock is seen in blue and purple surrounding the remnant. Image credit: NASA/CXC/MIT/UMass Amherst/M.D. Stage et al.

the Alfvén speed

$$v_A = \frac{B}{\sqrt{\mu_0 m_i n}}, \quad (1.3)$$

where B is the magnetic field, μ_0 is the vacuum permittivity, m_i is the ion mass.

Another important wave mode is the magnetosonic wave which can create shocks in plasmas. The group speed of magnetosonic waves is

$$v_{ms}^2 = \frac{v_A^2 + c_s^2}{2} \pm \frac{1}{2} \sqrt{(v_A^2 + c_s^2)^2 - 4c_s^2 v_A^2 \cos^2 \theta}, \quad (1.4)$$

where θ is the propagation angle in respect to the magnetic field, v_A is the Alfvén speed and c_s is the ordinary speed of sound. The speed of sound is defined as $c_s = \partial P / \partial \rho$, where P is the isotropic pressure and $\rho = m_i N$ the mass density

[Balogh and Treumann, 2013; Swanson, 1989]. For a magnetosonic shock to form the flow has to have magnetosonic Mach number $M_{ms} = \frac{V}{v_{ms}} > 1$. The \pm in the above equation gives equation to two magnetosonic wave modes: the fast magnetosonic wave mode v_{ms}^+ and the slow magnetosonic wave mode v_{ms}^- . Of the wave modes presented here, only the fast magnetosonic wave propagates perpendicular to the magnetic field. In other directions all three wave modes can exist and form shocks. Therefore there are three kinds of shocks: the fast, the slow and the Alfvénic shocks. In this work we are looking at the fast mode shock since the solar wind speed is faster than the magnetosonic speed, making the bow shock a fast type shock.

A shock around a supernova remnant Cassiopeia A is seen in Figure 1.1. Here, the collisionless shock has accelerated electrons to ultra-relativistic speeds producing synchrotron radiation visible in the x-ray [Koyama et al., 1995; Koo and Park, 2017].

The shock waves around supernova remnants are very efficient particle accelerators and are most likely the source of galactic cosmic rays [Blandford and Ostriker, 1978]. The particles are accelerated in a process called diffusive shock acceleration (DSA). When a high energy particle crosses the shock from upstream to downstream, it may get reflected back upstream from the turbulence and waves. Upstream the particle gets reflected off the upstream waves back to the shock, gaining energy in the process. Downstream it is reflected off collisions with slow downstream waves. The particle loses energy here as it overtakes slow waves but on average the particle gains energy. This process happens again until the particle has gained enough energy to escape as a cosmic ray. DSA can accelerate not only electrons but protons as well [Morlino and Caprioli, 2012]. A problem with DSA is that the initial particle energy required to enter the process is high, provoking the question: how can particles gain this energy in the first place? While this remains an open question, one solution is that ions could gain the sufficient energy by a mechanism called shock drift acceleration, which we will look in to later.

For a shock where the Mach number exceeds a critical limit, the shock becomes supercritical [Edmiston and Kennel, 1984; Kennel, 1987]. Such shocks are unable to slow down the flow fast enough with dissipation alone. Instead, supercritical shocks reflect a portion of the incoming ions back upstream.

1.3 Ion reflection

An important feature of a supercritical shock is its ability to reflect a portion of the incoming ions back upstream. This ability comes from the fact that supercritical

shocks are unable to slow down or heat the incoming flow fast enough. To deal with the excess energy the shock must have mechanics other than wave-particle interactions. A solution is to reject the excess portion of the incoming energy by reflecting some of the incoming plasma.

The efficiency of the ion reflection along with the shock geometry is dependent on the angle θ_{Bn} between shock normal vector \hat{n} and the upstream magnetic field \mathbf{B} . This angle is often defined to be an acute angle. Using θ_{Bn} we can distinguish two types of shocks: the quasi-parallel shock where $\theta_{Bn} < 45^\circ$ and the quasi-perpendicular shock where $\theta_{Bn} > 45^\circ$. What differentiates the two is that in quasi-perpendicular shocks the ions return to the shock accelerated by the convection electric field

$$\mathbf{E} = -\mathbf{V} \times \mathbf{B}. \quad (1.5)$$

In quasi-parallel shocks, the ions propagate along the magnetic field further upstream. The reflection off a quasi-parallel and quasi-perpendicular shock is drawn in Figure 1.2.

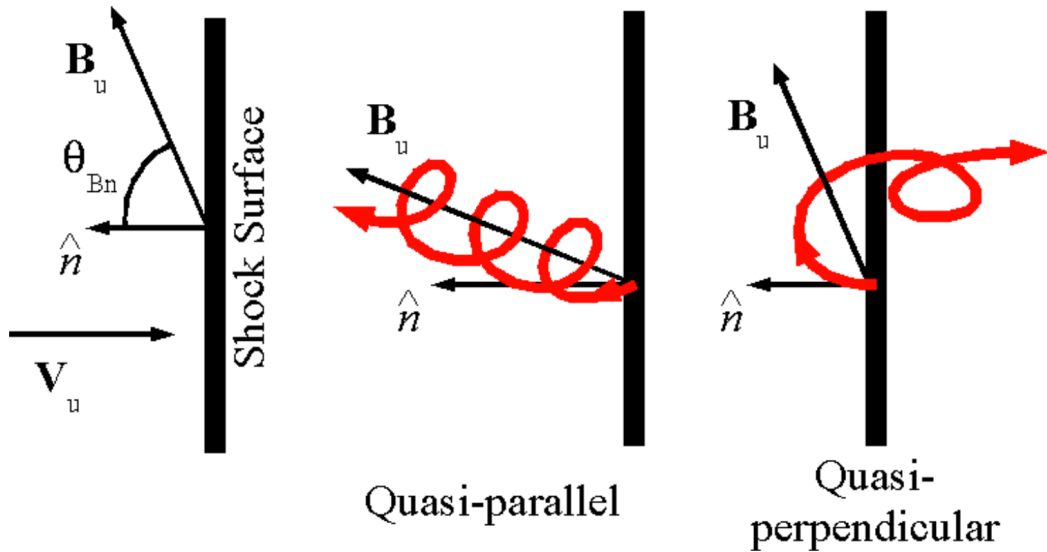


Figure 1.2: Ion reflection from quasi-parallel and quasi-perpendicular shock. Image credit: Schwartz et al. [2004]

A path of an ion as it is reflected from a perpendicular shock is drawn in Figure 1.3. Before hitting the shock itself, the ion encounters a region populated with reflected ions as well as incoming ions. This region is called the shock foot. After the shock foot, the ion encounters the shock ramp, which is a sudden increase in density and magnetic field. If the ion does not have enough energy to overcome

the magnetic field and the cross-shock electric potential, it is reflected back to the foot where it performs a gyration and returns to the ramp with more energy. The size of the foot is proportional to the ion gyroradius as the ions gyrate in an arch back to the shock. The reflected trajectories are spread to non-circular path by the acceleration the ion experiences by the convection electric field. As the ion returns, it now has enough energy cross the shock ramp. The ion now arrives to the downstream region where the magnetic field is compressed. Downstream the ion performs gyrations with decreased gyroradius as it travels further downstream.

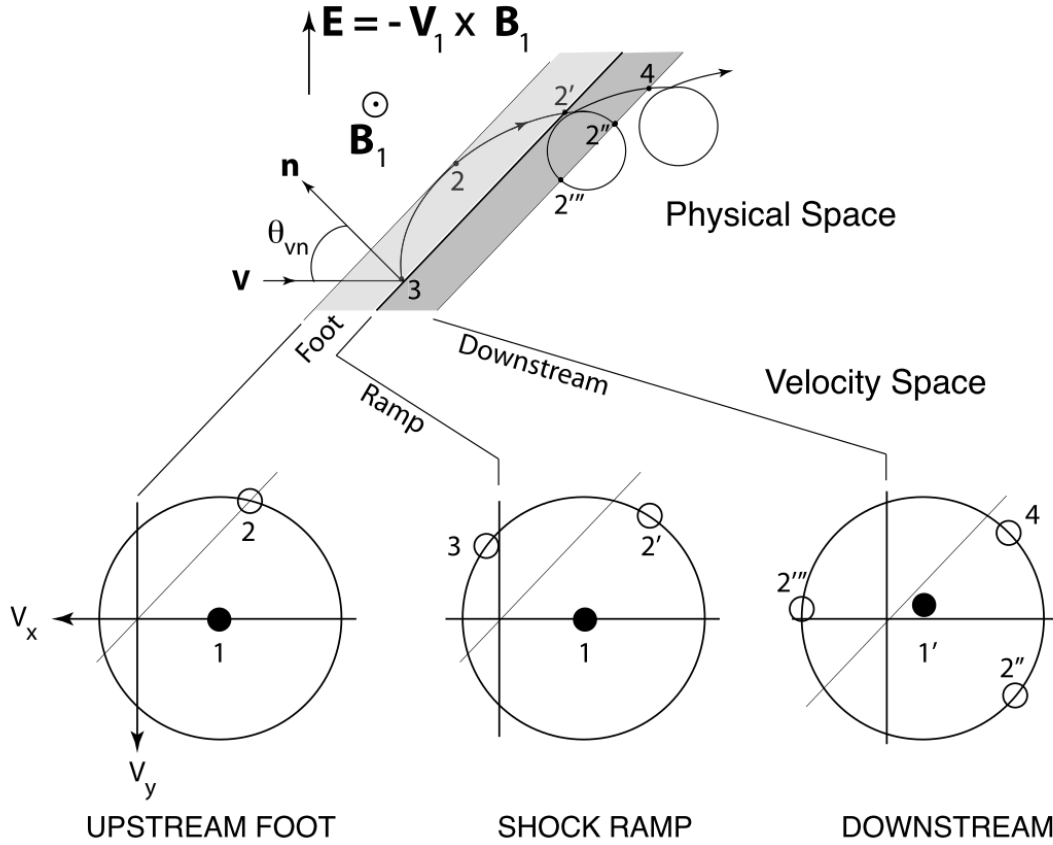


Figure 1.3: Ion reflection from the shock with the ion distribution function in velocity space from indicated locations in real space. The shock surface is drawn as a line in the velocity space figures. Image credit: Balogh and Treumann [2013]

Now we will look at velocity space v_x, v_y drawn in the bottom half of Figure 1.3. In the upstream, the ion is in the solar wind population drawn as the black dot population 1 in the figure. Upon hitting the shock, the ion is specularly reflected, which means the velocity component along the shock normal changes sign and the tangential component remains unchanged. The reflection can be seen in population 3, which mirrors the solar wind on the other side of the of the shock surface. The

ion then moves upward and gyrates in the solar wind. The ion moves along the drawn circle in velocity space. This circle is constant energy in the solar wind frame. The ion moves in the shock foot until it reaches the turning point. Here the ion's speed along the shock normal vector is zero. In the velocity space, the ion has now entered population 2, which has velocity just where the shock surface line is. The ion now continues towards the shock again eventually hitting and crossing it, seen as population 2'. In the downstream, the ion continues to gyrate forming the populations seen in the downstream panel of Figure 1.3.

1.4 Earth's bow shock

The solar wind flows with speed faster than the fast magnetosonic speed. As the solar wind hits a planetary magnetic field a bow shock forms [Sonett and Abrams, 1963]. The name bow shock comes from bow waves that form ahead of a bow of a ship as it sails in water. Rather than a ship moving through still water, the solar wind flows and hits seemingly stationary planets. In the frame of the solar wind, the bow shock appears to be moving, piercing through the solar wind, making the analogue to the bow waves more apparent. The Earth's bow shock has a hyperbolic curve shape and has its nose at about $14R_E$ in the direction of the Sun [Fairfield, 1971; Farris et al., 1991]. The location of the bow shock can vary with changing upstream conditions. For example when the Solar wind has higher Mach number, the shock is forced more towards Earth [Cairns and Lyon, 1995].

The bow shock is a thin layer of the order of $10^1 - 10^2$ kilometers [Schwartz et al., 2011; Svensson, 2018]. Behind the shock lies a turbulent magnetosheath. It is populated by shocked solar wind particles and a small amount of particles escaping from the magnetosphere below [Paschmann et al., 2005]. The magnetic field varies erratically in the magnetosheath. Behind the magnetosheath is the magnetopause where the pressure from the planetary magnetic field is balanced with the solar wind pressure. On the nightside of the Earth is the magnetotail where the magnetic field is significantly stretched away from Earth by the solar wind, see Figure 1.4.

The geometry of the shock is dependent on the angle θ_{Bn} between the upstream magnetic field \mathbf{B} and the shock normal vector $\hat{\mathbf{n}}$. The shock can be quasi-perpendicular or quasi-parallel depending on if $\theta_{Bn} > 45^\circ$ or $\theta_{Bn} < 45^\circ$ respectively. The difference can be seen in Figure 1.4, where the quasi-perpendicular side shock has a smooth and steep shock ramp whereas the quasi-parallel shock is uneven and turbulent. The bow shock is typically supercritical which means the shock is un-

able to slow down the flow enough with dissipation alone. Instead, excess energy is handled by reflecting a portion of incoming ions back upstream. The turbulent nature of the quasi-parallel side is caused by reflected ions that propagate back upstream along the magnetic field [Thomsen, 1985], forming a large foreshock region highlighted in dark red in Figure 1.4, whereas in the quasi-perpendicular shock they return to the shock.

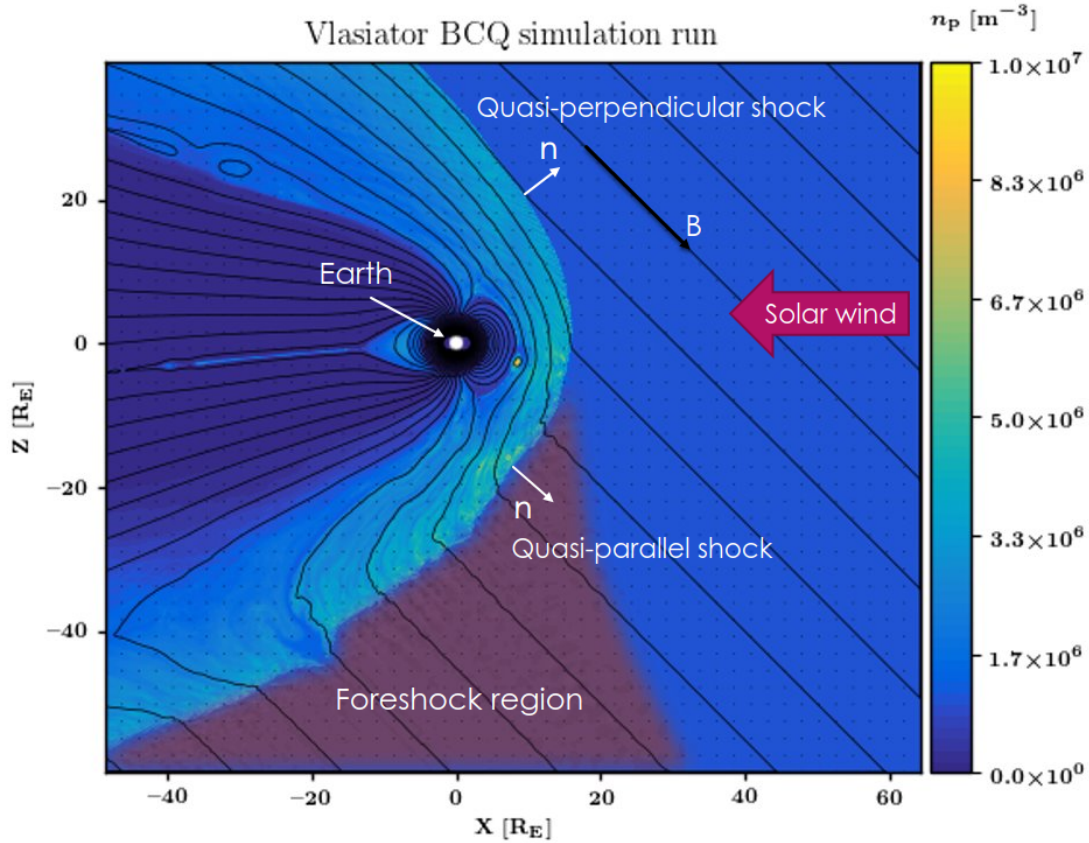


Figure 1.4: Earth's bow shock with solar wind coming from the right from a Vlasiator simulation. Foreshock region highlighted in dark red.

Since the solar wind exceeds the fast magnetosonic speed the shock is "fast" type shock where the magnetic field downstream of the shock increases. This is seen in spacecraft data in Figure 1.5. In the Earth's quasi-perpendicular bow shock before the shock ramp comes a region populated by both incoming solar wind ions and reflected ions called the shock foot. This is seen as a small increase in the magnetic field and density. After the foot comes the shock ramp which is a abrupt increase in magnetic field and density while the solar wind is slowed down. After the ramp there is a steep overshoot region where the magnetic field increases yet again followed by a undershoot region where it decreases. The overshoot and undershoot

are caused by currents in the shock ramp.

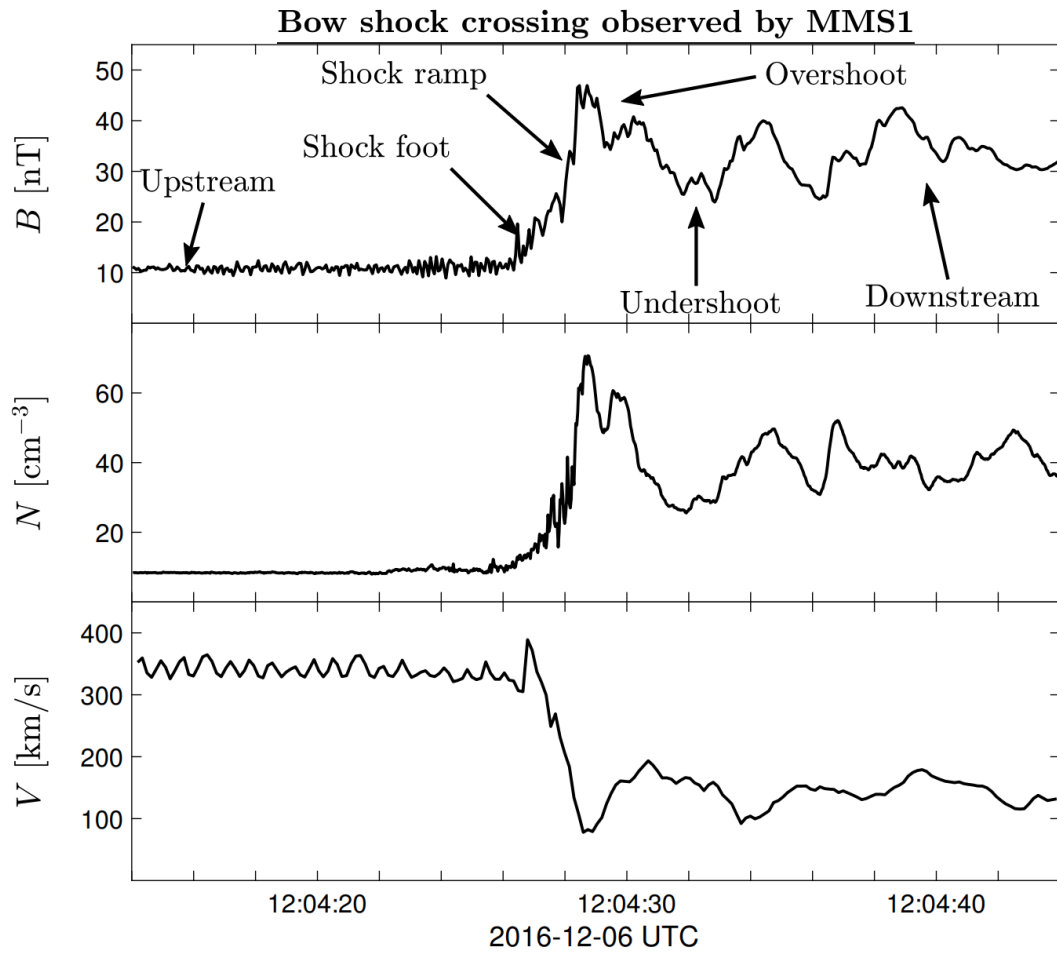


Figure 1.5: Spacecraft data from Magnetospheric Multiscale (MMS) mission crossing the quasi-perpendicular bow shock. Upper panel shows magnetic field magnitude with different regions of the shock shown. Middle panel shows electron number density. Bottom panel shows ion flow speed. Image credit: Johlander [2019]

2. Vlasiator

Global simulation of near-Earth space environment is a useful tool to help and complement spacecraft missions. Accurate simulation of such a system is a difficult task and many types of simulations have been used to solve this problem. Most popular of the simulation types has been magnetohydrodynamic (MHD) simulations where the MHD equations have been implemented in a computer simulation. These simulations can provide accurate results in large parts of the magnetosphere [Ridley et al., 2010]. MHD simulations do not simulate ion kinematics which means something more is needed to study regions where ion reflection is a large contributor.

In hybrid simulations, ions are modeled with a kinetic model while electrons are modeled as a fluid. In particle-in-cell (PIC) simulations the ions are represented as macroparticles for which the plasma kinetic equations are solved. These methods produce numerical noise which can be reduced by increasing the number of ions in the simulation. While this reduces the noise, it quickly also increases the computing time needed for the simulation.

Another way to do hybrid simulations is to not model the ions as particles but as distribution functions and use the Vlasov equation, which we will introduce later in the report, for their time evolution. These hybrid-Vlasov simulations require very large amounts of memory and computations to propagate the distribution functions. Vlasiator is a state-of-the-art hybrid-Vlasov simulation that can globally simulate the near-Earth space [Palmroth et al., 2018; Pfau-Kempf, 2016].

2.1 Simulation model

In space plasmas the dynamical state of system particles of species s at a time t can be described with a distribution function in position and velocity space $f_s(\mathbf{r}, \mathbf{v}, t)$ [Chen, 2016]. The distribution function represents phase space density of the species inside an 6-dimensional volume element of size $d^3\mathbf{x}d^3\mathbf{v}$ with time dt . Phase space density is drawn in Figure 2.1. Integrating $f_s(\mathbf{r}, \mathbf{v}, t)$ over velocity space gives the

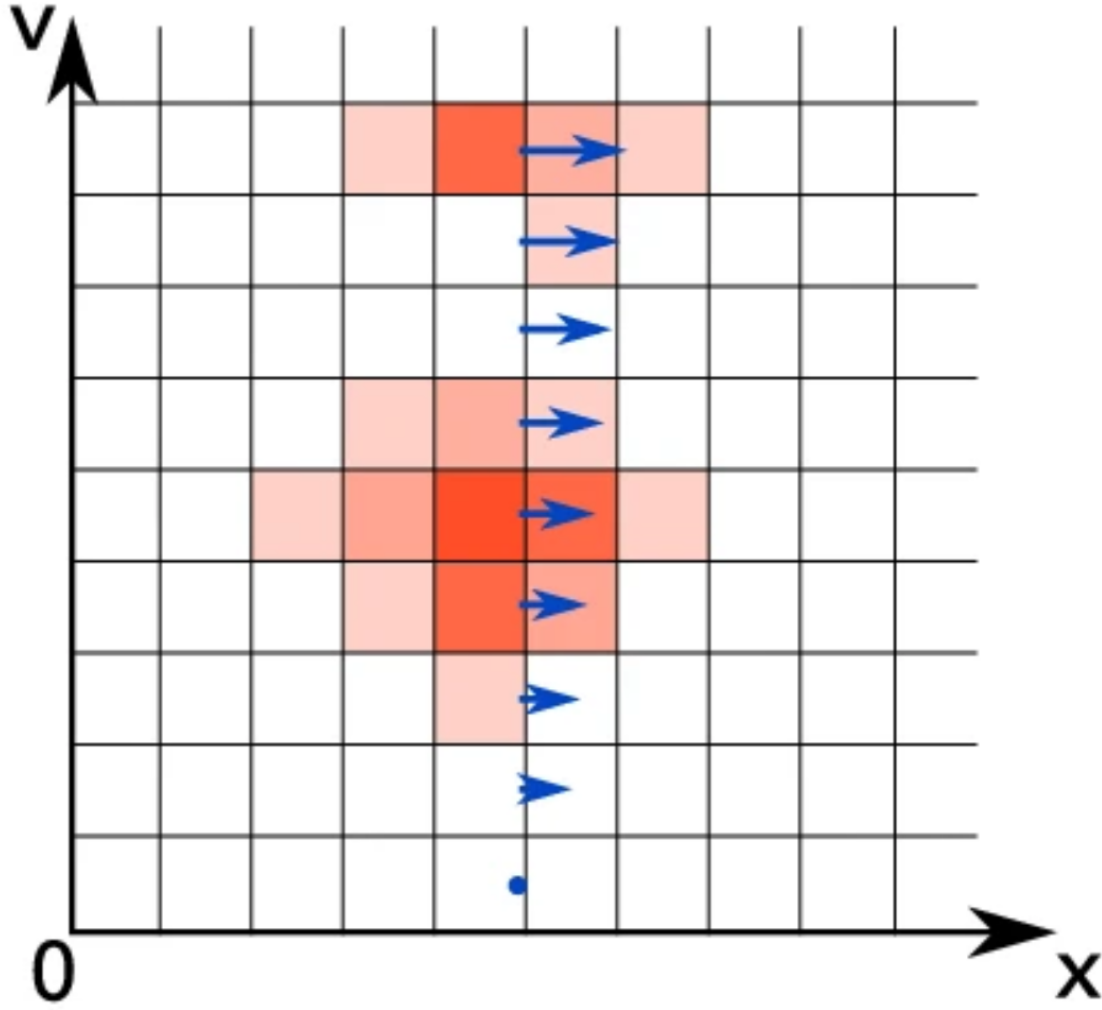


Figure 2.1: Phase space density drawn in Eulerian grid. Image credit: Palmroth et al. [2018]

particle number density $n_s(\mathbf{x})$ and integrating over both velocity and position space gives the total number of particles N_s .

It is important to know how $f_s(\mathbf{r}, \mathbf{v}, t)$ evolves with time. The distribution function has to satisfy the Boltzmann equation

$$\frac{\partial f}{\partial t} + \mathbf{v} \cdot \nabla f + \frac{\mathbf{F}}{m} \cdot \frac{\partial f}{\partial \mathbf{v}} = \left(\frac{\partial f}{\partial t} \right)_{\text{coll}}, \quad (2.1)$$

where \mathbf{F} is the force acting on the particles and the right side term is the time rate of change of f due to collisions. In collisionless plasmas, collisions between particles are negligible and therefore the only force acting on the particles is the Lorentz force

$\mathbf{F} = q \mathbf{E} + q \mathbf{v} \times \mathbf{B}$. The equation takes form

$$\frac{\partial}{\partial t} f(\mathbf{r}, \mathbf{v}, t) + \mathbf{v} \cdot \frac{\partial}{\partial \mathbf{r}} f(\mathbf{r}, \mathbf{v}, t) + \frac{q}{m} (\mathbf{E} + \mathbf{v} \times \mathbf{B}) \cdot \frac{\partial}{\partial \mathbf{v}} f(\mathbf{r}, \mathbf{v}, t) = 0. \quad (2.2)$$

This is called the Vlasov equation [Vlasov, 1961]. In simulations the fields in the Vlasov equation need to be solved using either Poisson's equation in electrostatic cases or Maxwell's equations in electromagnetic case. Vlasiator uses the Ampère-Maxwell's law without the displacement current. The electric field \mathbf{E} is closed using a generalized Ohm's law

$$\mathbf{E} = -\mathbf{V} \times \mathbf{B} + \frac{1}{qn_e} \mathbf{j} \times \mathbf{B}, \quad (2.3)$$

where \mathbf{j} is the electric current density. In Vlasiator, only ions are modeled with distribution functions whereas electrons are modeled as a charge neutralizing fluid. This makes Vlasiator a hybrid-Vlasov simulation. To account for the effects of the electrons, the generalized Ohm's law has the Hall term $\frac{1}{qn_e} \mathbf{j} \times \mathbf{B}$. The time evolution of \mathbf{B} is calculated using Faraday's law in a form

$$\Delta \mathbf{B} = -\Delta t \cdot \nabla \times \mathbf{E}. \quad (2.4)$$

In Vlasiator, the distribution function is propagated forward with a finite volume method in which the simulation domain is covered into a mesh consisting of a finite number of cells. The 6-dimensional space is split into Cartesian mesh in both position and velocity space. The ordinary space is 1D, 2D or 3D depending on the simulated case. Values for \mathbf{E} , \mathbf{B} , n and \mathbf{V} as well as other variables are stored for each spatial cell. The 3D velocity distribution function is stored at every \mathbf{r} spatial cell position forming a less dense grid in velocity space. The saved velocity cells can be seen in Figure 1.4 as black dots covering the whole figure. To boost computational efficiency, Vlasiator uses a sparse velocity grid, where portion of the velocity space is discarded if phase space density is below a chosen threshold $f < f_{\min}$. Storing the velocity distribution in a sparse grid reduces the amount of required velocity cells by a factor of 100 with little loss of accuracy [von Alfthan et al., 2014].

The velocity distribution function (VDF) at a point close to the quasi-perpendicular shock ramp is plotted in Figure 2.2. Here the upstream solar wind is seen as the spherical population intersected by the magnetic field direction line. On the left is a population of reflected ions forming a curved shape resembling a banana. Between the two mentioned populations are smaller populations of reflected ions. All of the

reflected populations have velocities perpendicular to the magnetic field, because the ions gyrate around \mathbf{B} after reflection. This gives an early indication that the ions are reflected in Vlasiator.

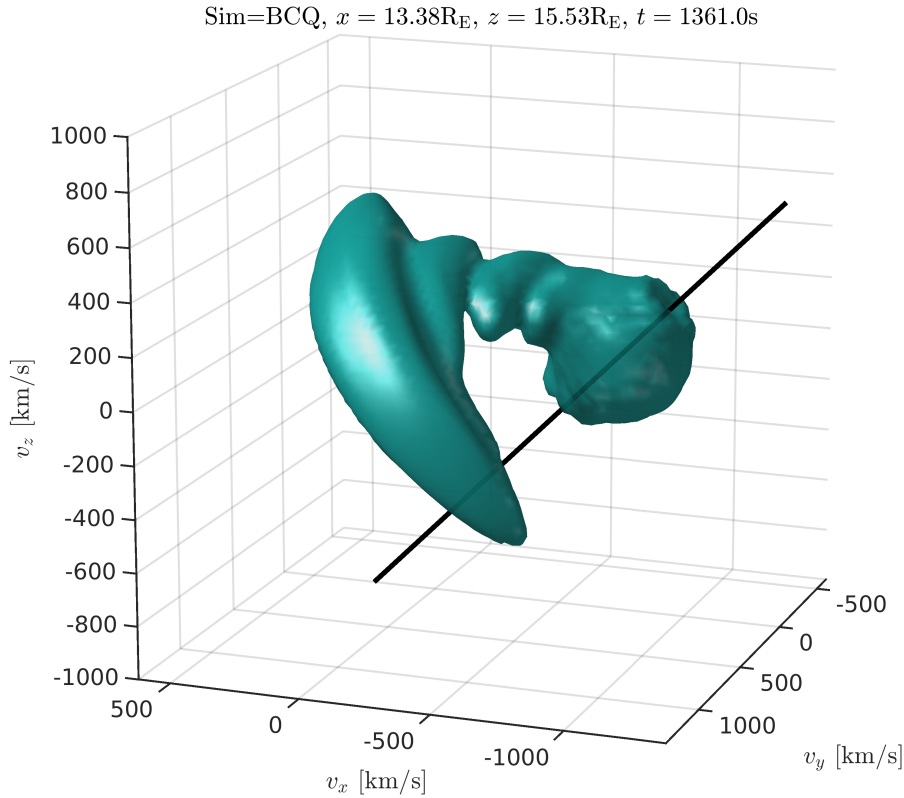


Figure 2.2: A velocity distribution function in 3D. The surface is where the phase space density is $f = 10^{-13} \text{ m}^{-6}\text{s}^3$. The direction of the magnetic field is drawn as a black line.

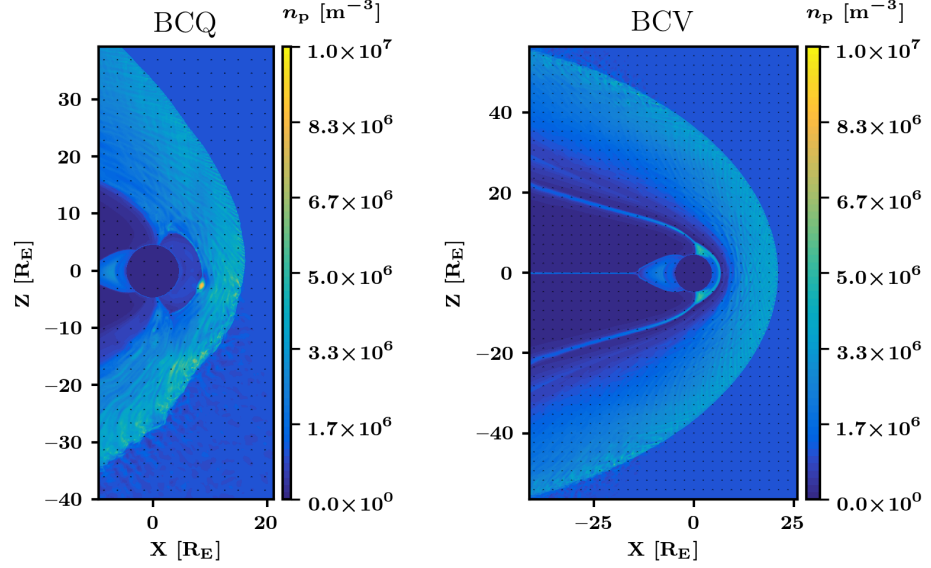
2.2 Simulation runs used

In this work we will use two separate Vlasiator simulations. While Vlasiator is capable of 6-dimensional simulations, the simulations we will use are both 5D: 2D in position space and 3D in velocity space. The properties of the simulations are listed in Table 2.1.

The two simulations have identical solar winds, with the exception of the direction of the magnetic field \mathbf{B} . Important to note is the coordinate system is chosen in a way where the colormaps are drawn in polar xz -plane, meaning we are looking at the system perpendicular to the ecliptic plane, as seen in Figure 2.3.

Table 2.1: Table of simulations used.

Simulation	BCQ	BCV
$\mathbf{B}[\text{nT}]$	$5 \times (\cos(45^\circ), 0, -\sin(45^\circ))$	$5 \times (0, 0, 1)$
Solar wind $n [\text{cm}^{-3}]$	1	1
Solar wind $V_x [\text{km s}^{-1}]$	-750	-750
Simulation time [s]	1437	2150

**Figure 2.3:** Colormaps of the two Vlasior simulations used in this work. On the left panel is the BCQ simulation and on the right panel is the BCV simulation.

The locations for the velocity distribution functions are visible as black dots. Many timesteps of both simulations were used but the general shape of the shock in the simulations remains as pictured.

In simulation BCV, seen in the right panel of Figure 2.3, the magnetic field is purely northward, pointing northward perpendicular to the ecliptic plane, causing the bow shock to be symmetrical in the z -direction. The shock is also almost completely quasi-perpendicular with only little quasi-parallel regions at the left side of the figure ($X \lesssim -25R_E$). In simulation BCQ, seen in the left panel of Figure 2.3 the magnetic field points towards the Sun southward in a 45° angle to the Earth-Sun line, causing the shock to have clear quasi-perpendicular and quasi-parallel sides. The quasi-parallel side has a large foreshock region whereas the quasi-perpendicular side has distinct shock ramp.

2.3 This work

While the Earth’s quasi-parallel bow shock has been the subject of many Vlasiator studies [e.g., Kempf et al., 2015; Turc et al., 2018; Battarbee et al., 2020], the quasi-perpendicular bow shock has not been studied in Vlasiator with such detail. The goal of this thesis is to study how are ions reflected (in what way and how efficiently) in the quasi-perpendicular bow shock in Vlasiator. In Chapter 3, we will derive expressions for velocities of ions reflected from the quasi-perpendicular bow shock and use these to estimate reflection in different models to investigate which models fit the observed reflected ion populations. In Chapter 4, we will study the properties of the bow shock and ion dynamics, such as ion reflection efficiency, at the shock. In Chapter 5, we will summarise the results of the previous chapters and give conclusions about the results.

3. Reflected ion populations

3.1 Specular reflection

Supercritical shocks are unable to slow down the solar wind fast enough with dissipation so a portion of the incoming ions are reflected back upstream. It is common in shock physics to assume that ions are reflected off a shock by specular reflection, where only the shock normal component of the velocity changes sign and the tangential velocity is preserved. The incoming ions experience the shock ramp as an impenetrable wall [Balogh and Treumann, 2013] and get reflected. In quasi-perpendicular shocks, the reflected ions gyrate around the magnetic field, being accelerated in the process.

The reflected ions play a major role in the downstream heating process and affect the structure of the shock in timescale of ion gyroperiod. The reflected ions are also a possible source for populations of upstream ions near the boundary of the foreshock called field-aligned beam (FAB) ions [Burgess et al., 2012]. The ions that are reflected multiple times are accelerated with each reflection. This process is called the shock drift acceleration (SDA). Eventually these ions reach the end of the quasi-perpendicular shock where they continue gyrating with the magnetic field forming FABs. It is therefore important to know in detail, how are ions reflected.

In this section we will investigate how are ions reflected off the Earths quasi-perpendicular bow shock in Vlasiator.

3.1.1 Reflected ion velocities

To study whether the ion reflection at the bow shock follows specular reflection or not, we need expressions for the velocities of the reflected ions. This was done by Schwartz et al. [1983] using the deHoffman-Teller frame. The downside of the deHoffman-Teller frame is that it breaks down when θ_{Bn} approaches 90° . For this reason a more convenient frame is the normal incidence (NI) frame commonly used

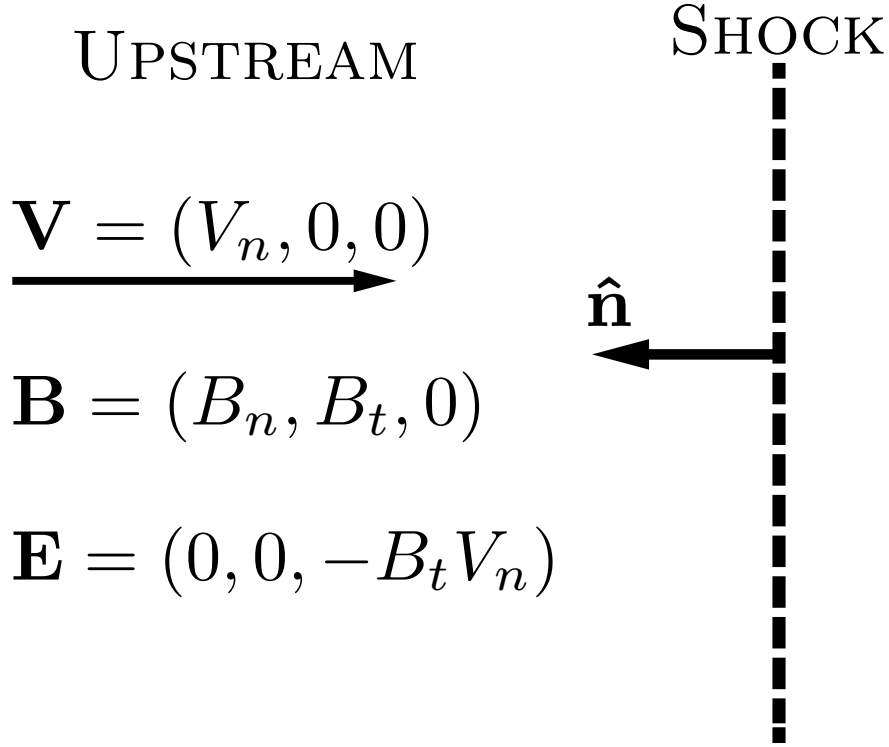


Figure 3.1: An illustration of normal incidence frame. The shock is shown as the dashed line with the normal vector drawn from it. The upstream velocity, magnetic field and the electric field are shown. Adapted from Johlander [2019].

in shock physics which is valid even when $\theta_{Bn} = 90^\circ$. In normal incidence frame, see Figure 3.1, the upstream plasma velocity is along the shock normal vector. The expressions for reflected ion velocities in normal incidence frame will be derived next.

We choose a coordinate system where the plasma flow velocity is

$$\mathbf{V} = (V_n, 0, 0) \quad (3.1)$$

the magnetic field in the upstream

$$\mathbf{B} = (B_n, B_t, 0), \quad (3.2)$$

and the electric field $\mathbf{E} = -\mathbf{V} \times \mathbf{B}$

$$\mathbf{E} = (0, 0, -B_t V_n). \quad (3.3)$$

There is a constant stream of plasma heading towards the shock at a speed of V_n .

Assuming specular reflection, right after the reflection the ion has a velocity

$$\mathbf{v}(0) = (-V_n, 0, 0). \quad (3.4)$$

Using Newton's second law and the Lorentz force

$$\mathbf{F} = q(\mathbf{E} + \mathbf{v} \times \mathbf{B}) \quad (3.5)$$

we get three equation of motions

$$\begin{cases} \ddot{x} = -\frac{q}{m}B_t\dot{z} \\ \ddot{y} = \frac{q}{m}B_n\dot{z} \\ \ddot{z} = \frac{q}{m}(B_t\dot{x} - B_n\dot{y} - B_tV_n), \end{cases} \quad (3.6)$$

where the double dot means time derivative twice and single dot means time derivative once. Integrating \ddot{x} over time yields

$$\dot{x} = -\frac{q}{m}B_t \int \dot{z} dt' = -\frac{q}{m}B_t z + C. \quad (3.7)$$

From initial conditions we get $\dot{x}(0) = -V_n$ and $z(0) = 0$. Now the previous integral becomes

$$\dot{x} = -\frac{q}{m}B_t z - V_n. \quad (3.8)$$

Similarly integrating \ddot{y} over time yields

$$\dot{y} = \frac{q}{m}B_n z. \quad (3.9)$$

Now we can use these to calculate \ddot{z} in equation (3.6)

$$\ddot{z} = \frac{q}{m} \left(-\frac{q}{m}B_t^2 z - V_n B_t - \frac{q}{m}B_n^2 z - B_t V_n \right) \quad (3.10)$$

$$= -\frac{q^2}{m^2}(B_t^2 + B_n^2)z - \frac{2q}{m}(V_n B_t). \quad (3.11)$$

Using gyrofrequency

$$\omega_{ci} = \frac{q}{m}B \quad (3.12)$$

and $B^2 = B_n^2 + B_t^2$, we get a differential equation

$$\ddot{z} + \omega_{ci}^2 z + \frac{2q}{m}V_n B_t = 0. \quad (3.13)$$

We can solve the equation using initial conditions $\dot{z}(0) = 0$ and $z(0) = 0$

$$z = \frac{2B_t V_n \frac{q}{m}}{\omega_{ci}^2} (\cos(\omega_{ci} t) - 1). \quad (3.14)$$

Time derivative of equation (3.14) yields us the z -component of the reflected ion velocity

$$v_z = \dot{z} = -\frac{2B_t V_n \frac{q}{m}}{\omega_{ci}} \sin(\omega_{ci} t). \quad (3.15)$$

We can derive this further by using the equation for gyrofrequency in (3.12)

$$v_z = -2 \frac{B_t}{B} V_n \sin(\omega_{ci} t) \quad (3.16)$$

We can calculate v_x and v_y using the derived z in equation (3.14) in equations (3.8) and (3.9)

$$v_x = \dot{x} = -\frac{2B_t^2}{B^2} V_n (\cos(\omega_{ci} t) - 1) - V_n \quad (3.17)$$

and

$$v_y = \dot{y} = \frac{2B_t B_n}{B^2} V_n (\cos(\omega_{ci} t) - 1). \quad (3.18)$$

We can simplify the velocities further by using $\sin \theta_{Bn} = B_t/B$ and $\cos \theta_{Bn} = B_n/B$

$$\begin{cases} v_x = -2 \sin^2(\theta_{Bn}) V_n (\cos(\omega_{ci} t) - 1) - V_n \\ v_y = \sin(2\theta_{Bn}) V_n (\cos(\omega_{ci} t) - 1) \\ v_z = -2 \sin(\theta_{Bn}) V_n \sin(\omega_{ci} t). \end{cases} \quad (3.19)$$

We have now expressions for the velocity of reflected ions. These expressions will next be used to compare with the observed reflected ion populations in Vlasiator.

3.1.2 Transformation to the simulation frame

We now adopt the notation of \mathbf{v} being the velocity of a reflected ion in the simulation frame and \mathbf{v}' being the ion velocity in the normal incidence frame and given by equation (3.19). To compare with the reflected ion populations in Vlasiator we need to transform these expressions back to the simulation frame and coordinate system. First the reflected ion velocities need to be rotated back to the simulation coordinate system. The simulation coordinate system is represented by $\hat{\mathbf{x}}, \hat{\mathbf{y}}, \hat{\mathbf{z}}$ and the shock coordinate system by $\hat{\mathbf{x}}', \hat{\mathbf{y}}', \hat{\mathbf{z}}'$. From Johlander et al. [2016], $\hat{\mathbf{x}}' = \hat{\mathbf{n}}$, $\hat{\mathbf{z}}' = \frac{\hat{\mathbf{n}} \times \mathbf{B}}{|\hat{\mathbf{n}} \times \mathbf{B}|}$ and

$\hat{\mathbf{y}}' = \hat{\mathbf{z}}' \times \hat{\mathbf{n}}$. The rotation to the simulation coordinate system can then be done by

$$\mathbf{A}^{-1}\mathbf{v}', \quad (3.20)$$

where \mathbf{A} is the rotation matrix

$$\mathbf{A} = \begin{pmatrix} \hat{n}_x & \hat{n}_y & \hat{n}_z \\ \hat{y}'_x & \hat{y}'_y & \hat{y}'_z \\ \hat{z}'_x & \hat{z}'_y & \hat{z}'_z \end{pmatrix}. \quad (3.21)$$

To move back to the simulation frame we use

$$\mathbf{v} = \mathbf{v}' + \mathbf{V}_{\text{NIF}}, \quad (3.22)$$

where \mathbf{V}_{NIF} is the velocity of the normal incidence frame given by Schwartz [1998]

$$\mathbf{V}_{\text{NIF}} = \mathbf{V} - (\mathbf{V} \cdot \hat{\mathbf{n}} - V_{sh})\hat{\mathbf{n}}, \quad (3.23)$$

where V_{sh} is the velocity of the shock, which we assume to be zero unless stated otherwise. Now with the expressions for velocity and the frame and coordinate transformation we have the tools to estimate specular reflections in Vlasiator simulations.

3.1.3 Estimating specular reflection

Now we use the Vlasiator BCV simulation, which is in the xz -plane and has a purely northward magnetic field along the z -axis. The solar wind speed is 750 km s^{-1} towards the left along the x -axis. A velocity distribution function from the nose of the bow shock at $z = 0$ and $x = 21R_E$ is shown in Figure 3.2. Since the magnetic field is northward and $\hat{\mathbf{n}}$ points straight towards the Sun at the peak of the shock, $\theta_{Bn} = 90^\circ$. The velocity distribution function is from just upstream of the shock which is why there is a distinct solar wind velocity population centered around $v_x = -750 \text{ km s}^{-1}$ in the xy -plane. The velocities of the reflected ions form the other population curving around the solar wind beam. In the xz -plane the reflected population is located around and to the right of the solar wind.

The expressions for ion velocities in equation (3.19) are each dependent on the angle between the normal vector and magnetic field θ_{Bn} , and the ion gyrophase $\omega_{ci}t$. When θ_{Bn} is known, a curve can be drawn for a range of gyrophases on top

of the velocity distribution function to where specularly reflected ion populations would be and compare that to the actual reflected ion populations. In Figure 3.2 a dashed line is drawn for $\theta_{Bn} = 90^\circ$ and $\omega_{ci}t$ from 0 to 2π . This does not take into account the fact that, for a quasi-perpendicular shock, the ion does not complete the whole gyration. Because of this, the velocity populations of reflected ions can only be found at the part of the circle where the ions are upstream of the shock.

For a more accurate estimation we can analyze the movement of the ion numerically. We use Euler method to integrate the path of a reflected ion, using equation (3.19), until it returns to the shock. A more advanced integration method is not necessary as Euler method is sufficiently accurate for this work. This method provides only the part of the reflection circle where the ion is upstream of the shock, meaning the equations are solved when $x > 0$. In Figure 3.2 this is drawn as the solid line.

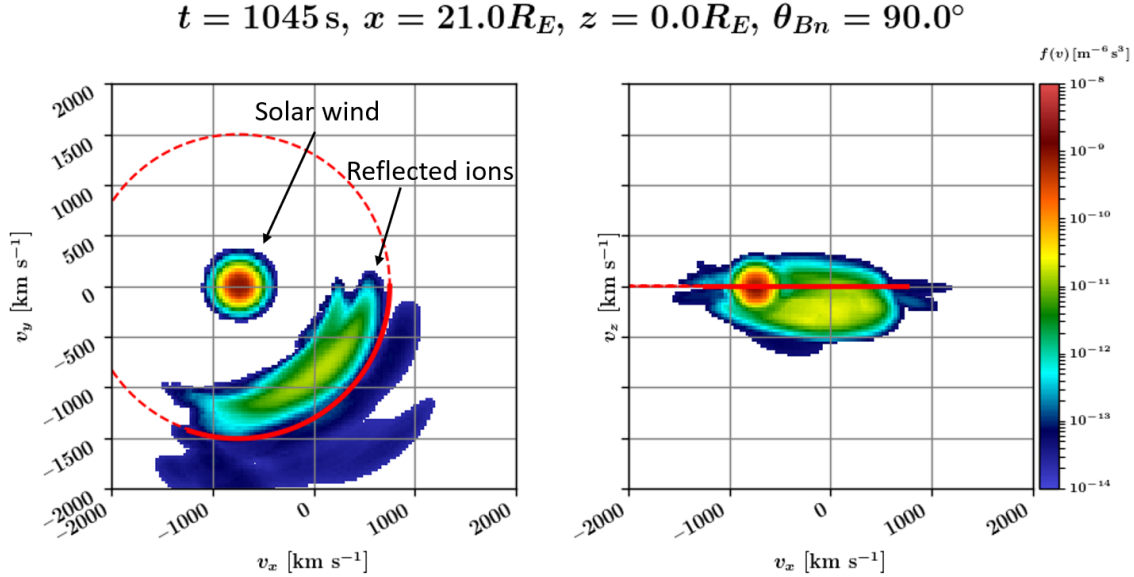


Figure 3.2: Estimations for specular reflection on top of a velocity distribution function from Vlasiator BCV simulation. The analytically calculated circle is plotted as the dashed line and the numerically calculated circle up until the first reflection is plotted as the continuous line.

In Figure 3.2, both the full circle and the numerically calculated part of the circle are plotted on top of a VDF from Vlasiator simulation. The plot of the simulation projects the whole VDF to the two planes. This is not a true projection of the VDF but it does indicate where there are ions. We can see that in the xy -plane the population follows the numerically calculated section of the circle well but is well inside the circle. In xz -plane the circle is just a line at $v_z = 0$. The x -extent of the continuous line, i.e. the numerically calculated estimate, is close to the width

of the simulated population. From both planes it can be seen that the Vlasiator simulation population is nearly, but not perfectly, specularly reflected.

This estimate works well when θ_{Bn} can easily be seen from the simulation, for example at the front of the shock where $\theta_{Bn} = 90^\circ$ such as in Figure 3.2. At other parts of the shock, estimating θ_{Bn} is increasingly hard which leads to inaccuracies in the reflection estimation. For accurate estimation we need to find a way to determine the shock normal vector at arbitrary part on the shock.

3.2 Determination of the shock normal vector

Since the expressions in equation (3.19) are all dependent on θ_{Bn} , the normal vector $\hat{\mathbf{n}}$ must be known to use these. We will use a method where $\hat{\mathbf{n}}$ is calculated from the shape of the bow shock for given coordinates. The point of the shock ramp can be estimated for a number of lines of the colormap by iterating the density from right to left until the density is above twice the solar wind value $n > 2n_{sw}$ [Battarbee et al., 2020]. Since the quasi-perpendicular shock is quite smooth this method finds the shock ramp well. Next a curve can be fitted to these points. A fourth degree polynomial fit with only even terms was used in this work

$$x = A + Cz^2 + Ez^4. \quad (3.24)$$

Two simulations with curves fitted to the bowshock can be seen in Figure 3.3, one for BCQ simulation and one for BCV. In the left panel the curve is fitted to half of the shock. This is because in the BCQ simulation the magnetic field, as seen in Table 2.1, causes the shock to be visibly asymmetric with the quasi-perpendicular bow shock being smoother than the quasi-parallel bow shock. In the left panel of Figure 3.3 the curve fit of the shock starts to visibly deviate quickly when $z < 0$.

A tangential vector $\hat{\mathbf{t}}$ of the shock curve can be used to calculate the normal vector. The tangential vector

$$d\mathbf{t} = \begin{pmatrix} dx \\ dz \end{pmatrix} \propto \begin{pmatrix} x' \\ 1 \end{pmatrix} \quad (3.25)$$

can be rotated 90° clockwise to get the normal vector at any point of the curve

$$d\mathbf{n} = \begin{pmatrix} 0 & 1 \\ -1 & 0 \end{pmatrix} \cdot \begin{pmatrix} x' \\ 1 \end{pmatrix} = \begin{pmatrix} 1 \\ -x' \end{pmatrix}, \quad (3.26)$$

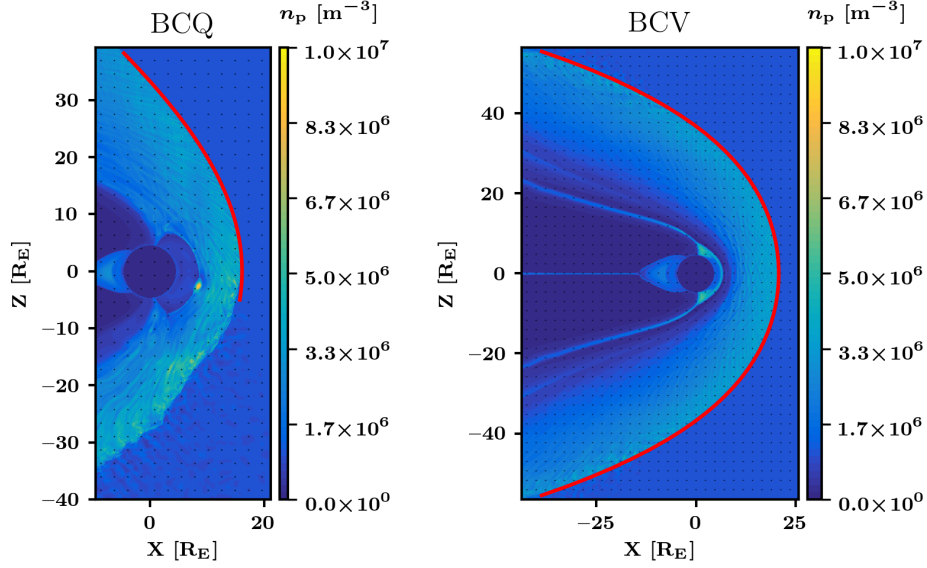


Figure 3.3: The calculated estimates of the shock plotted on top of two Vlasiator simulations. On the left is the BCQ simulation and on the right is the BCV simulation. The estimates are plotted as the red line.

which is then used to obtain the unit normal vector $\hat{\mathbf{n}}$. This rotation ensures that $\hat{\mathbf{n}}$ always points upstream. The normal vector can then be calculated using the derivative of the function used to fit the curve

$$x' = 2Cz + 4Ez^3. \quad (3.27)$$

We can now estimate specular reflection at any point of the shock. In Figure 3.4 the specular reflection is estimated at $x = 8.0R_E$, $z = 30.0R_E$, where $\theta_{Bn} = 45.6^\circ$. In the xy -plane the estimate is a good fit with a approximately matching shape of the $v_y < 0$ ion velocity population. It is clear that there are more mechanisms going on than just a one specular reflection as there is a clear population on the $v_y > 0$ side as well. In the xz -plane the specular reflection estimate fits the first population quite well although the estimation is a little too wide for the population in the x -axis. Here again there is another population with a greater velocity parallel to the magnetic field suggesting the presence of other mechanisms producing the other populations.

In Figure 3.5 we can see a specular reflection estimate in the same 3D VDF as in Figure 2.2. Here, the estimate follows the curvature of the population well but is further away from the solar wind population.

With the a way to calculate $\hat{\mathbf{n}}$ at an arbitrary point of the shock we can now start looking for ways of estimating ion velocity populations other than a single

$$t = 1045 \text{ s}, x = 8.0R_E, z = 30.0R_E, \Delta n \approx 0.1R_E, \theta_{Bn} = 45.6^\circ$$

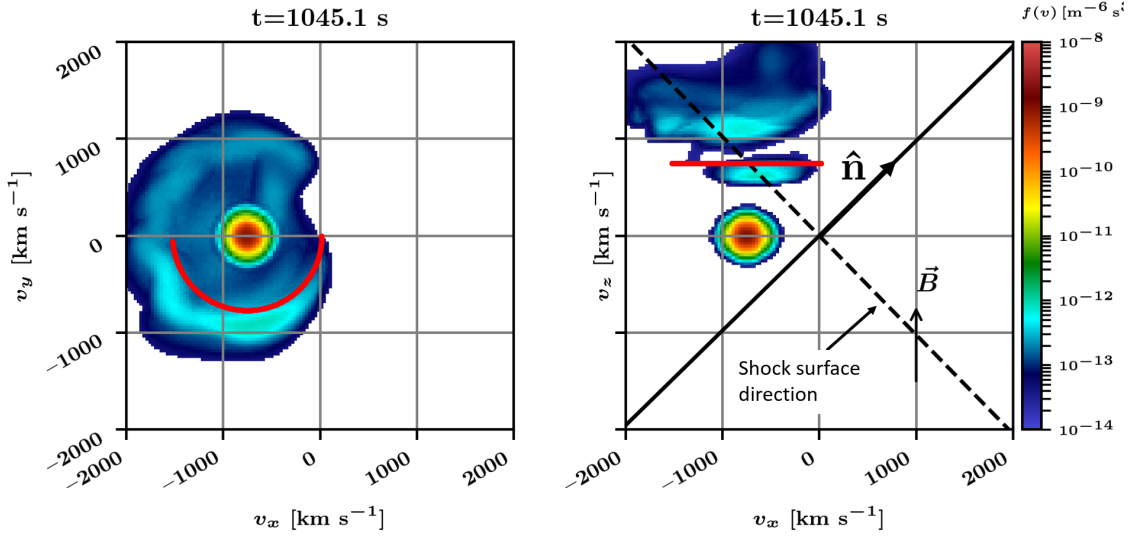


Figure 3.4: Estimates for specular reflection where $\theta_{Bn} \neq 90^\circ$ plotted on top of a velocity distribution function from BCV simulation. Normal vector as solid line and tangential vector as dashed line are drawn on the v_x - v_z -plane as a crosshair. Direction of the magnetic field is shown as an arrow. Δn is the distance to the polynomial fit of the curve in the direction of \hat{n} .

specular reflection.

3.3 Beyond specular reflection

Previously in this work, ions have been assumed to get specularly reflected off a static shock to get estimates for the reflection. While the estimates are good, we will also look into other mechanisms. In this chapter we will inspect velocity distribution functions from four different locations from the two simulation runs. This will allow us to study ion reflection at multiple parts of the shock. These points are shown in Figure 3.6. In these panels it can be seen that there are local properties of the shock that in some case can affect the results.

3.3.1 Reflection in other frames

Downstream frame reflection

In our previous estimates in the NI-frame, the shock is static wall the particles hit and get reflected off. In reality, the particles penetrate the shock by their gyroradius as the reflection is not an instantaneous reflection. Because of this we will look in to the case where the ions are specularly reflected but in a frame moving with

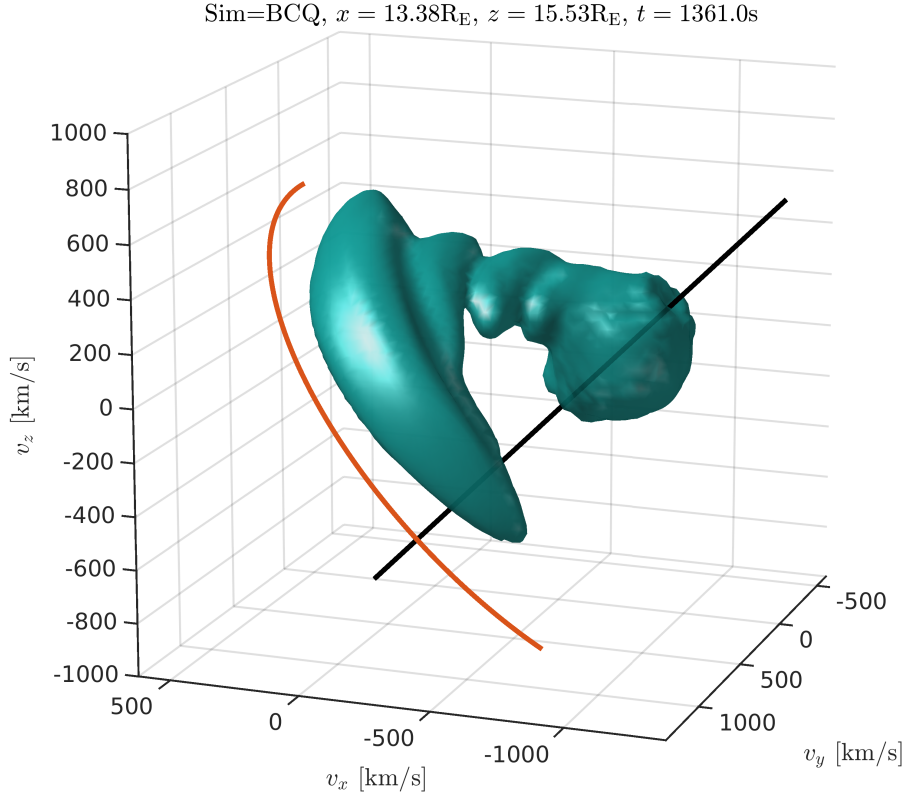


Figure 3.5: Estimate for specular reflection in a 3D plot. Same VDF as in Figure 2.2 with estimate for specular reflection in NI frame.

the downstream plasma, instead of reflection in the NI-frame. This assumption was used by Caprioli et al. [2015] studying ion acceleration at non-relativistic collisionless shocks. This assumption is analogous to bouncing a ball to the back of a moving truck instead of a wall. From the NI-frame this downstream frame reflection works similarly as before in equation (3.4) with the velocity changing sign but now it also loses velocity from the moving frame

$$v(0) = -V_n + 2V_D, \quad (3.28)$$

where V_D is the downstream velocity. V_D needs to be added two times since the frame needs to be first transformed into the downstream frame for the reflection and then back into NI-frame. The downstream velocity is determined by the density compression ratio $r = N_D/N_U$, where N_U is the upstream density, so that $V_D = (1/r)V_n$. Here we use a compression factor of 4 which is often observed at the

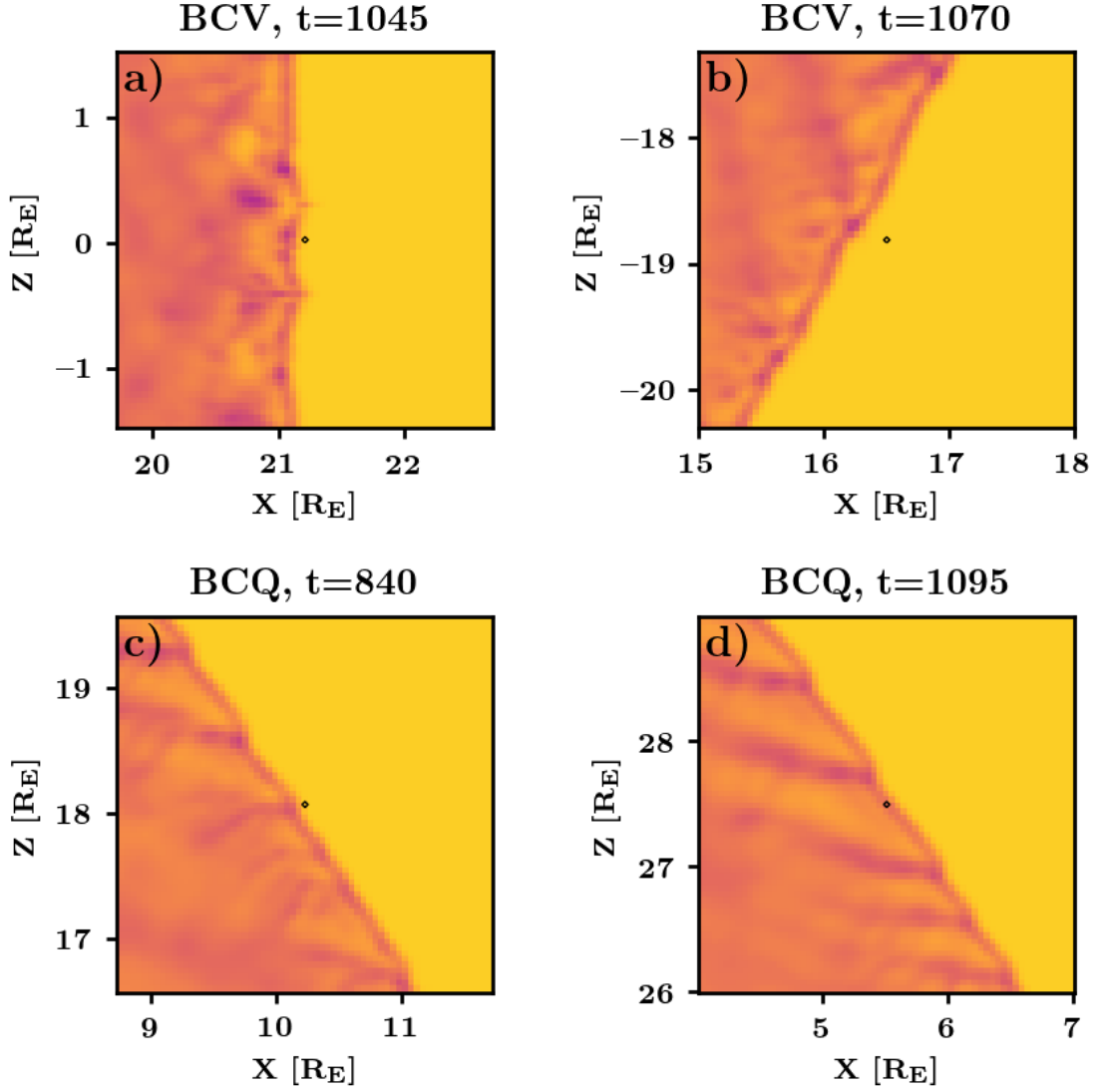


Figure 3.6: Locations of four points used in this chapter. Simulation name and time of the simulation are indicated above each image.

Earth's bow shock [Formisano et al., 1973]. We also observe similar compression factor in Vlasiator, see Chapter 4.

Specular reflection estimates in both the NI-frame and the downstream frame are shown in Figure 3.7. The VDF is at coordinates $x = 21.2 R_E, z = 0.0 R_E$, as shown in Figure 3.6a. The path in velocity space of the ion reflected in the downstream frame is much shorter than its NI-frame counterpart in both planes and in the xz -plane is a little closer to the solar wind population at $v_x = -750 \text{ km s}^{-1}$. A reflected ion population is present in the close proximity of the estimates with the downstream frame estimate being right on top of the population and the NI-frame

estimate being on the edge of the main reflected population.

$$t = 1045 \text{ s}, x = 21.2R_E, z = 0.0R_E, \Delta n \approx 0.5R_E, \theta_{Bn} = 90.0^\circ$$

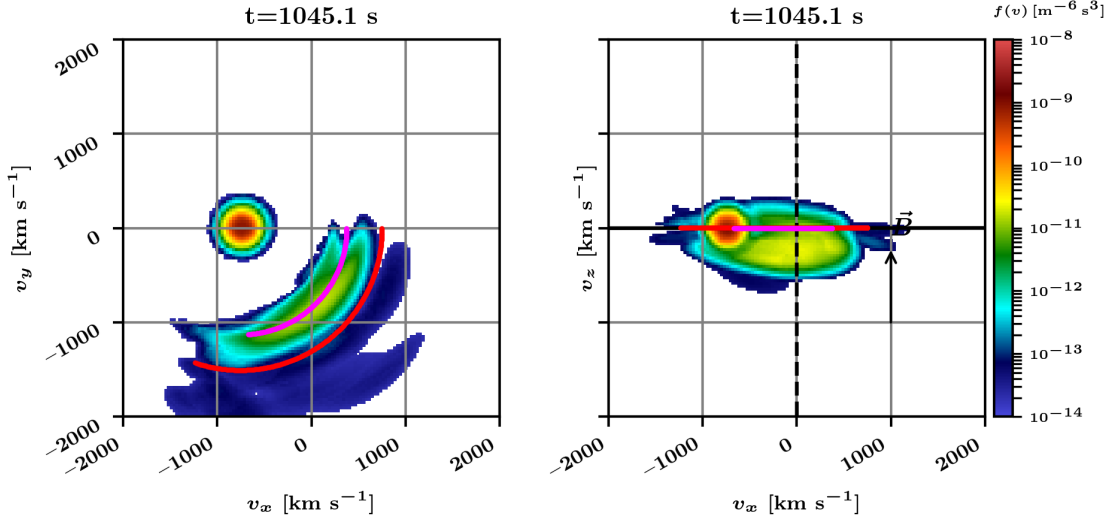


Figure 3.7: Ion reflection upstream of the perpendicular shock in two frames. The reflection in the NI-frame is drawn as the red line and the downstream frame is drawn as the magenta line. Same format as Figure 3.4.

Like before, the specular reflection estimates calculated in two frames are plotted in Figure 3.8. The point of the VDF is shown in Figure 3.6b. This time the distance to the shock is greater than before, about $0.25R_E$, which is comparable to the gyroradius of a reflected ion. The shock is clearly in the quasi-perpendicular region with $\theta_{Bn} = 62.7^\circ$. The ion populations appear smaller than in previous figures. This is because the VDF is close to the turning point of the ions where the trajectories of the reflected ions start to turn back to the shock. In an ideal case there is only one beam of reflected ions in this region [Sckopke et al., 1983], which is why the population in the VDF is only slightly elongated compared VDFs in previous figures where there ideally would be two beams and the solar wind beam. In Figure 3.8 estimates of the specular reflection are a good fit to the main reflected population. There is a distinct, less dense population in addition to the denser reflected population. This is likely reflected ions that have undergone a second reflection. We will investigate this population further later in the report.

Hall frame

We will now investigate a case in which the electric field vanishes. This frame can be found with the generalized Ohm's law (equation 2.3) by moving the frame in

$$t = 1070 \text{ s}, x = 16.5R_E, z = -18.8R_E, \Delta n \approx 0.1R_E, \theta_{Bn} = 62.7^\circ$$

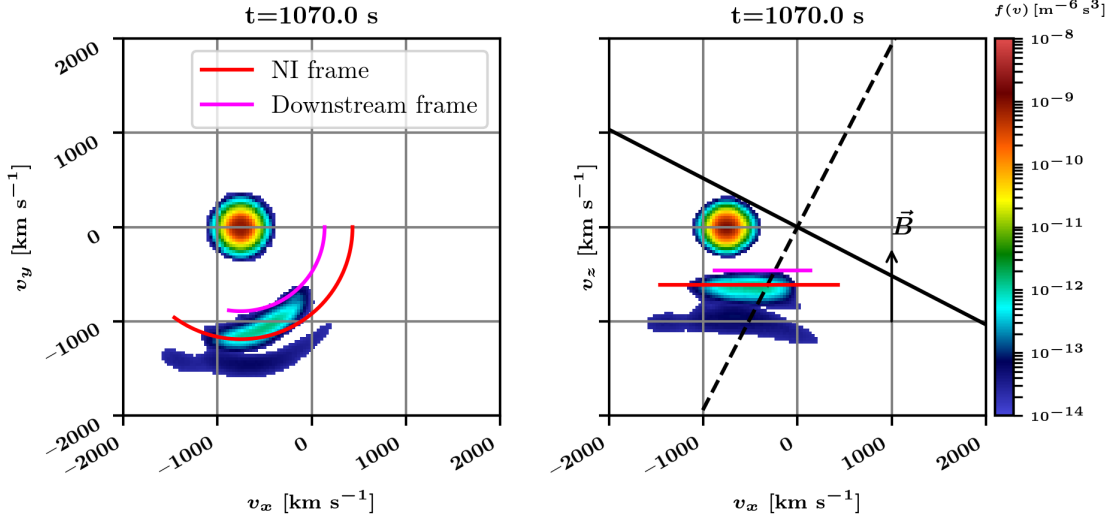


Figure 3.8: Ion reflection upstream of the quasi-perpendicular shock. Same format as Figure 3.7.

frame of reference of the electrons at the shock according to the Hall term $\frac{1}{qn_e} \mathbf{j} \times \mathbf{B}$, hence the name Hall frame. In this frame, only the magnetic field can change how the particle moves [Battarbee et al., 2021], which causes the ions to be reflected by magnetic mirroring. The frame is similar to downstream frame as it is also moving with the downstream flow speed but it has an additional velocity caused by moving with the electron flow. The frame is moving in $\hat{\mathbf{z}}'$ -direction with an approximate velocity of

$$V_e \sim -\frac{1}{qn_e} j, \quad (3.29)$$

where the current density can be approximated from Ampère's law

$$j \sim \frac{B_d - B_u}{\Delta x \mu_0}, \quad (3.30)$$

where B_d and B_u are the magnetic field in the downstream and upstream respectively, Δx is the thickness of the shock and μ_0 vacuum permeability. Here we use $B_d = 15 \text{ nT}$, $B_u = 5 \text{ nT}$ approximated from Vlasiator. For the shock thickness we use $\Delta x = 300 \text{ km}$ which is the velocity cell resolution for the simulations used. Using these values we get $V_e = 66.2 \text{ km s}^{-1}$ and $j = 26.5 \text{ nA/m}^2$.

Ion reflection in this frame can be estimated using the same method as before. In this frame the reflection in the v_x happens according to the downstream frame reflection (equation 3.28) but also has an additional velocity $v_z(0) = -2V_e$.

Figure 3.9 shows reflection estimates for both downstream frame and Hall

$$t = 1045 \text{ s}, x = 21.2R_E, z = 0.0R_E, \Delta n \approx 0.5R_E, \theta_{Bn} = 90.0^\circ$$

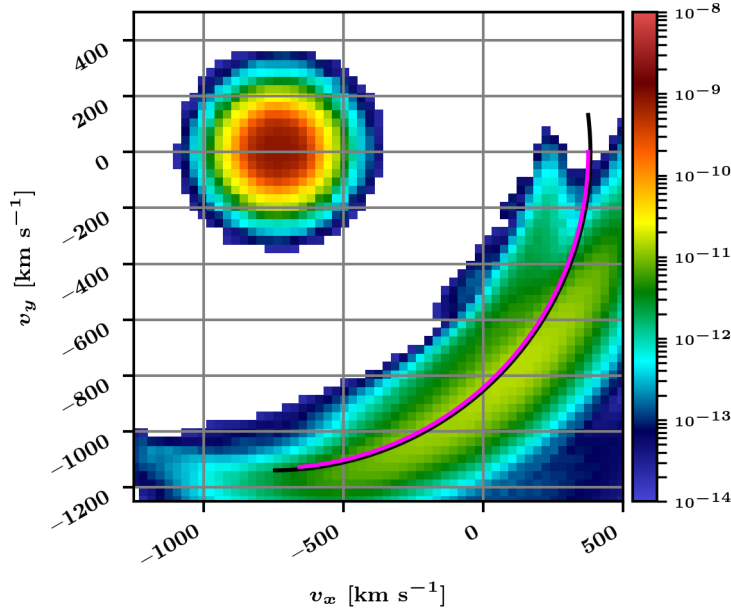


Figure 3.9: Ion reflection in the upstream of the quasi-perpendicular shock with the downstream frame (magenta) and Hall frame (black) estimates. Same VDF as Figure 3.7.

frame reflection. The difference between the two is small, however the Hall frame estimate allows for a wider range for the reflected population, as can be seen from the black Hall frame estimate that extends further than the downstream frame estimate. In the v_x - v_z -plane the estimate is shifted by $-2V_e$. The normal component of the electric field in the shock is mostly caused by the Hall term. We can calculate the Hall term to investigate the electric field resulting in $E_n \approx 1 \text{ mV/m}$ which is small compared to typical electric fields found in the quasi-perpendicular bow shock that are around 10 mV/m [Walker et al., 2004]. The calculated electric field is in line with electric fields found in the simulation runs used as seen in Section 4.1. E_n is roughly the same as E_x as shown later in Section 4.2. The small electric field is due to the spatial resolution of the simulation run. With a better resolution the shock would be thinner and the current would be higher. This would cause the Hall frame reflection to be more distinct from the downstream frame reflection. Hence in the future, finer resolution Vlasiator simulations could be used to further study ion reflection in the Hall frame.

Intermediate frame

In many VDFs, the observed ion population have been between the specularly reflected and the downstream reflection estimates. This is why we adopted another estimate where the frame is exactly between the downstream and NI frame so that the ions are reflected from a surface moving with half the speed of the downstream flow speed $V_{IF} = 1/8V_n$. This reflection model will be referred as the intermediate case estimate.

In Figure 3.10 all three frames are drawn on top of a BCQ simulation VDF. The location of the VDF is shown in Figure 3.6c. Although the location is upstream of the shock, it is right next to a local wave-like structure almost hitting it from the side. This may cause ions to be reflected at a surface where $\hat{\mathbf{n}}$ is very different from the $\hat{\mathbf{n}}$ of the estimated shock that is just a polynomial curve with no local features. Because of this even if the ions would be specularly reflected some of them would not fit the estimates. This is possibly seen in the right panel where there are two distinct populations as well as the solar wind beam. The specular reflection estimates are accurate with the less energetic one, which means the other population could be ions reflected from the wave. In the left panel, there is a population seemingly spreading from the solar wind beam. We speculate that these could be ions gyrating downstream of the shock, temporarily crossing into upstream.

We can see that the intermediate case estimate fits the reflected ion population very well in the xy -frame, where the NI frame and downstream frame are a good fit but the center of the population is between them. In the xz -frame two populations are present with the all estimates fitting the less energetic one pretty much equally well. From now on, the intermediate case will be drawn in the figures along with the NI frame and the downstream frame.

3.3.2 Two reflections

In the previous VDFs, there have often been smaller, less dense ion populations with higher velocities in addition to the main reflected ion population. The higher velocities indicate that these could be reflected ions that, upon hitting the shock, are reflected again and thus accelerated further. Only a portion of the ions hitting to shock get reflected and this portion gets smaller and smaller with each reflection. These reflected ions gain energy via shock drift acceleration and eventually either cross the shock downstream or escape upstream.

We will assume that the second reflection is a specular reflection just like the

$$t = 840 \text{ s}, x = 10.2R_E, z = 18.1R_E, \Delta n \approx 0.1R_E, \theta_{Bn} = 75.8^\circ$$

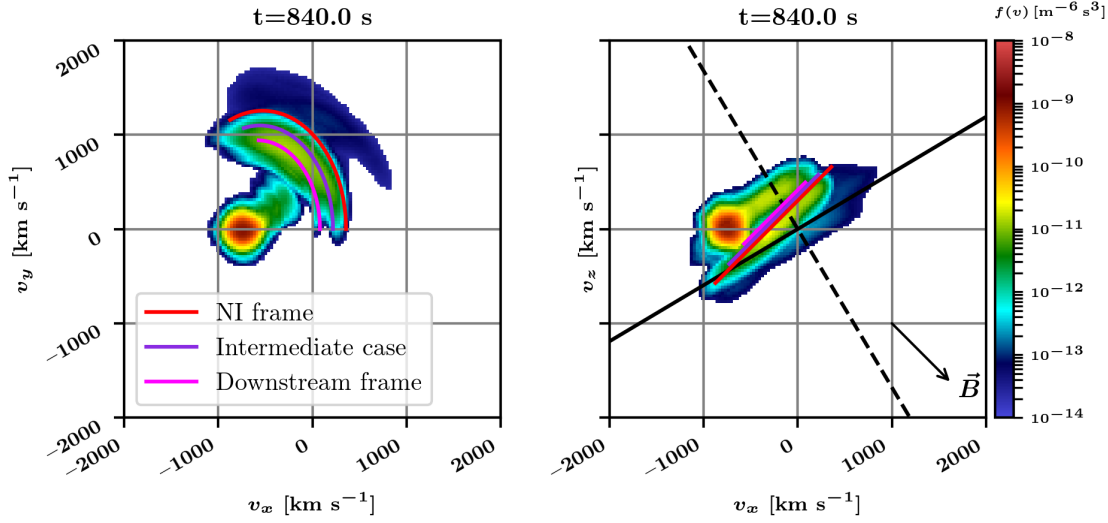


Figure 3.10: From BCQ simulation with the same format as Figure 3.8 with the addition of an intermediate case reflection.

first. However, this is just an assumption as the second reflection would not have to be specular just because the first is. Unlike before, it is impossible to solve the second reflection analytically as equation (3.19) does not have an analytical solution to $x = 0$ as it reduces to $\cos(x) = x$, which is a transcendental equation. This means it is necessary to use a numerical method. We will use the same method as before, where the path of the reflected ion is calculated from equation (3.19) using Euler method, but now changing the velocity of the ion according to equation (3.4) as it hits the shock. In this case this is

$$v_x \rightarrow -v_x + 2V_S, \quad (3.31)$$

where v_x is the normal component of the ion velocity and V_S is the velocity of the moving frame: 0 for NI-frame, $V_n/4$ for the downstream frame and $V_n/8$ for the intermediate frame.

The number of possible reflections depends on θ_{Bn} . Assuming specular reflection, the reflected particles escape upstream to the foreshock region when $\theta_{Bn} < 39.9^\circ$ [Schwartz et al., 1983]. When $\theta_{Bn} = 90^\circ$, the ion can go through very large number of reflections as it never gains parallel speed, which is needed to escape the shock. For $39.9^\circ < \theta_{Bn} < 90^\circ$ the ions return to the shock and can be reflected again gaining energy, and repeating the process many times. Using the same numerical method as before, where the path of the reflected ion is integrated with the Euler

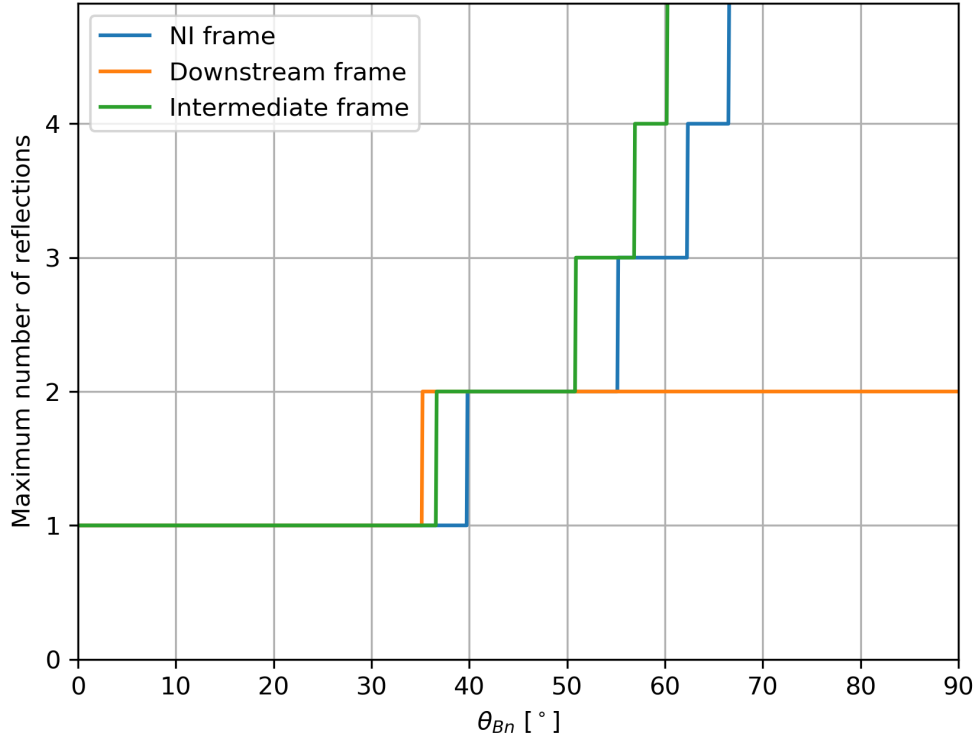


Figure 3.11: Maximum number of reflections possible for an ion that is always reflected off the shock as a function of θ_{Bn} in three frames.

method using equation (3.19), the number of specular reflections until an ion, that is always reflected when hitting the shock, escapes upstream is plotted in Figure 3.11. We can see that in the NI-frame, the ion can be reflected only once for θ_{Bn} between 0° and 39.9° as expected. The required angle for a new reflection gets smaller and smaller forming a curve that approaches infinity as $\theta_{Bn} \rightarrow 90^\circ$. In the intermediate frame the ion loses energy from the moving frame, making the number of possible reflections higher for a given θ_{Bn} compared to the NI-frame.

For the downstream frame it can be seen that only two reflections are ever possible. The ions gain energy as they gyrate back to the shock but lose energy as they are reflected off a moving frame. In the case of the downstream frame, after the second reflection the ion never gains enough energy to be reflected again and is unable to continue the reflection process. As the third reflection happens, the ion velocity v_x stays negative because $|v_x| < |2V_S|$ in equation (3.31) and the ion continues moving downstream. Ions being reflected more than two times, like in [Caprioli et al., 2015], is therefore not consistent with repeated specular reflections

in the downstream frame.

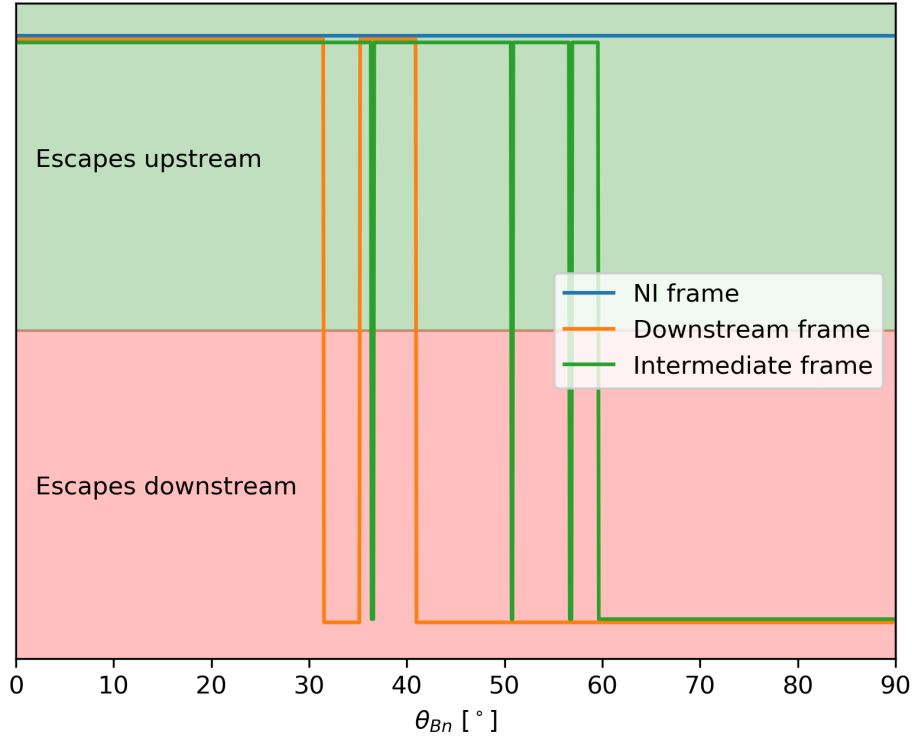


Figure 3.12: The direction in which an ion that is always reflected when hitting the shock escapes as a function of θ_{Bn} . The green side means escapes upstream and the red side means escapes downstream.

When integrating the path of an ion that is reflected every time it encounters the shock using the Euler method, as is done here, the ion always escapes eventually upstream in the NI frame. However in the downstream and intermediate frames the ion can escape downstream if $v_x < 0$ after the reflection. The direction in which the ion escapes is plotted in Figure 3.12. In the downstream frame the ion has a period of downstream escapes before the first reflection. After the reflection it has escapes upstream until $\theta_{Bn} \gtrsim 40^\circ$ after which it always escapes downstream. In the intermediate frame the ion has spikes of downstream escapes at around θ_{Bn} values where a new reflection becomes possible. For $\theta_{Bn} > 60^\circ$ the ion can only escape downstream.

In Figure 3.13 is the same VDF as in Figure 3.7, but this time showing two reflections in three frames. The second reflection estimates are plotted as dashed lines. Though the VDF is a messy one the intermediate frame estimate is a good fit to the reflected population. The first reflection estimate lies in the middle of the

main reflected population in the xy -plane while the second reflection estimate hits a less dense population further away. In the other two frames the second reflections do not represent any of the populations in the VDF with the same accuracy.

$$t = 1045 \text{ s}, x = 21.2R_E, z = 0.0R_E, \Delta n \approx 0.5R_E, \theta_{Bn} = 90.0^\circ$$

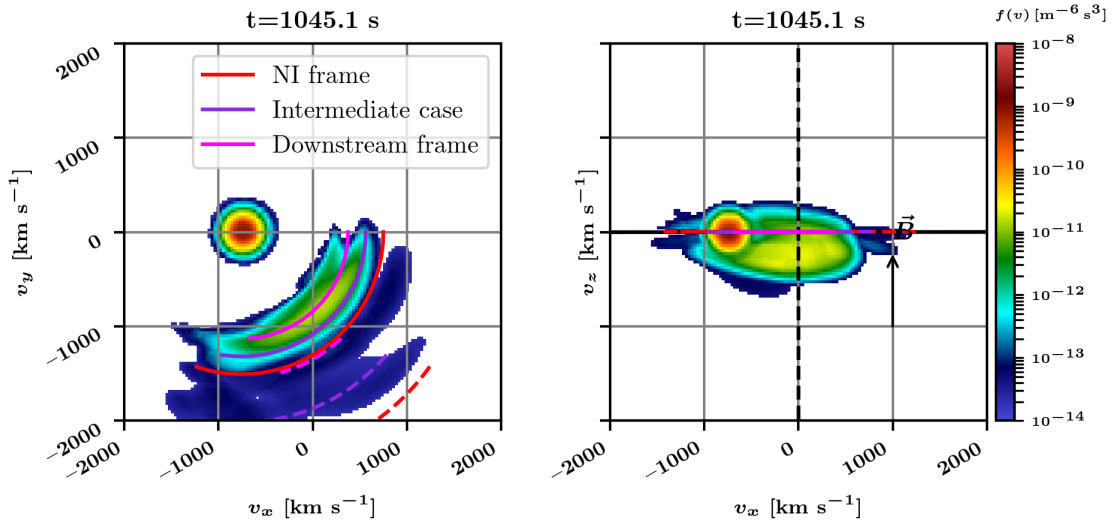


Figure 3.13: Same as Figure 3.7, now also shows three frames and second reflections as dashed lines.

Figure 3.14 is the same VDF as in Figure 3.8 with three frames and estimates for two reflections. Here, in the xy -plane, the NI frame estimates seem to fit the population the best. The second reflection of the NI frame estimate goes right through the higher-energy less dense population. In the xz -plane the intermediate frame estimate seems closer to the reflected population as it almost hits the second reflection population. In this case the NI frame estimate is good for the perpendicular velocity, while the intermediate frame estimate is better for the parallel speed.

In our observations it has been a recurring theme that in the xy -plane the estimates for specular reflection have been good while in the xz -plane the estimates have not been as good. In Figure 3.15 is a downstream population right after the shock. The location of this VDF is in Figure 3.6d. However, in the xy -plane we can see a clear downstream population where the estimates are not very good at all, which is expected because the gyration center is different in the downstream compared to the upstream where the estimates are calculated. In the xz -plane we see that the NI frame estimate fits a population well for the first and the second reflection. As the ions get reflected they penetrate the shock by some amount. The reflected population in the xz -plane may be these ions that have been reflected but

$$t = 1070 \text{ s}, x = 16.5R_E, z = -18.8R_E, \Delta n \approx 0.1R_E, \theta_{Bn} = 62.7^\circ$$

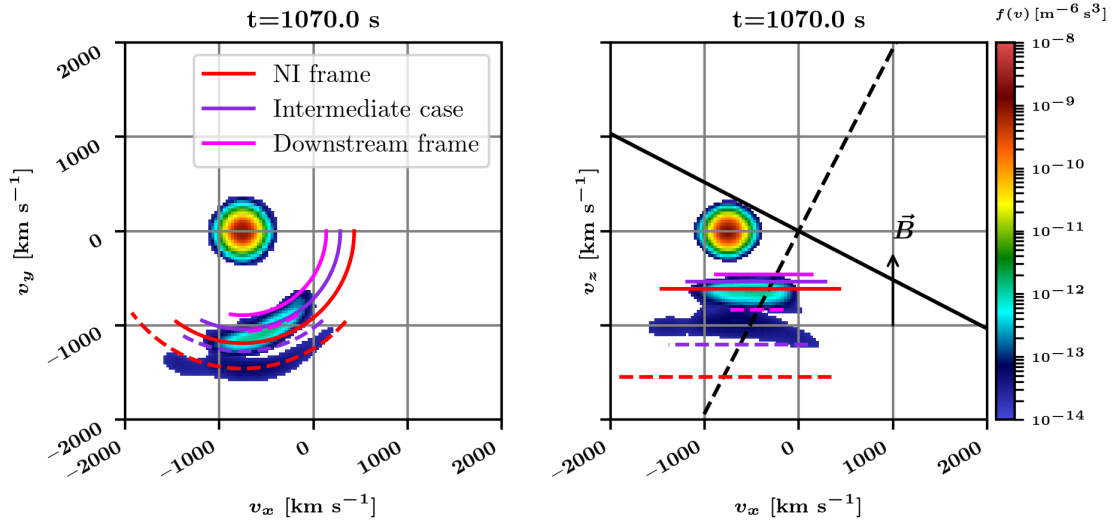


Figure 3.14: Same VDF as Figure 3.8 with three frames and two reflections.

are downstream. These ions have gained parallel acceleration in the direction of the magnetic field which we see in the VDF.

$$t = 1095 \text{ s}, x = 5.5R_E, z = 27.5R_E, \Delta n \approx -0.1R_E, \theta_{Bn} = 81.1^\circ$$

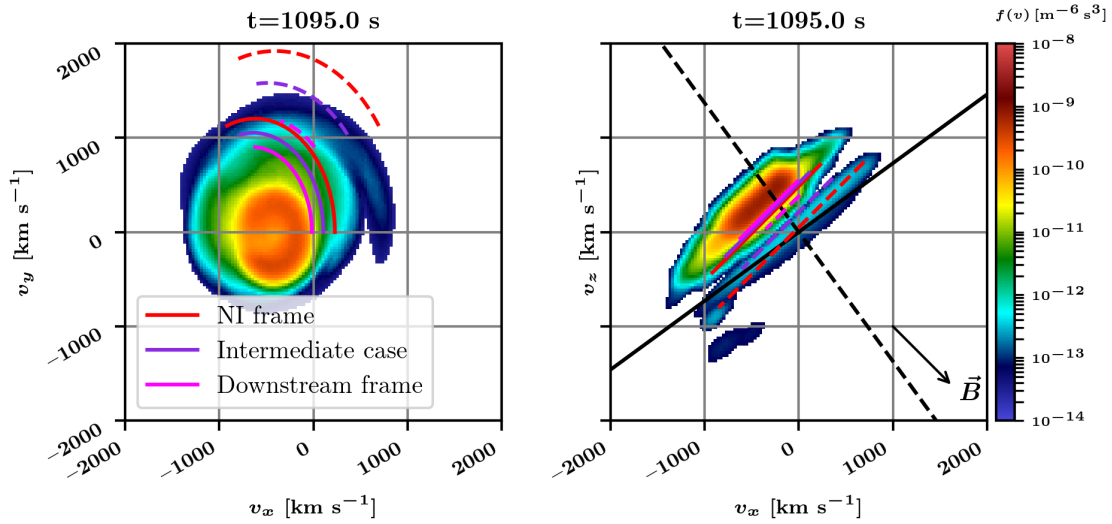


Figure 3.15: Same format as Figure 3.13 for a downstream point in BCQ simulation.

3.4 Traversing the shock, analysis of one quasi-perpendicular shock crossing

Previously we have looked at single points from different parts of bow shocks. In this section we will take a closer look at a single point as it traverses through the shock. In Vlasiator the shock moves sunward with time so a single simulation cell can act as a virtual spacecraft moving through the shock. This is not unlike real spacecraft shock crossings where the shock moves over a spacecraft. However in Vlasiator the shock only moves forward as time progresses whereas the real bow shock moves a few Earth radii back and forth depending on the upstream plasma conditions. We will take a look at four points in time to study how the VDF evolves while crossing the shock. The shock at these four times is pictured in Figure 3.16. The path of the virtual spacecraft goes near a wave like structure, almost surfing the wave as it moves on the shock surface, after which it slowly crosses the shock. An estimate of the virtual spacecraft's apparent trajectory, as the shock waves move along the shock, is drawn in Figure 3.17. In the ~ 20 seconds the crossing takes, the shape of the shock evolves quite a lot, which is why the trajectory is not a straight line but rather a curve.

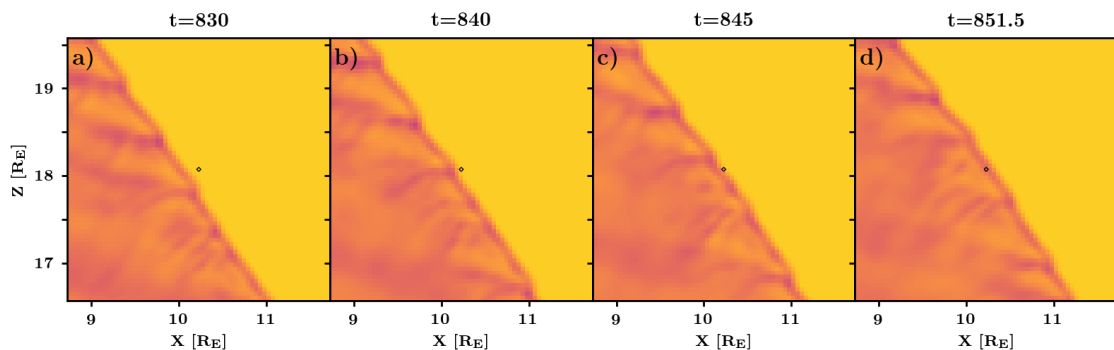


Figure 3.16: Virtual spacecraft crossing the quasi-perpendicular shock at four different times. Time is expressed in seconds.

The simulation used in this section is the BCQ simulation, see Table 2.1. The location of the shock crossing is chosen so $\theta_{Bn} \approx 75^\circ$, making the virtual spacecraft cross a clearly quasi-perpendicular shock. In this section we will only use the intermediate frame for our estimates. The first and second specular reflection estimates are shown in the VDFs.

The first VDF at $t = 830$ s is still rather far from the shock. Estimating from Figure 3.16a the distance is about $0.2R_E$ which is very close to the ion gyroradius

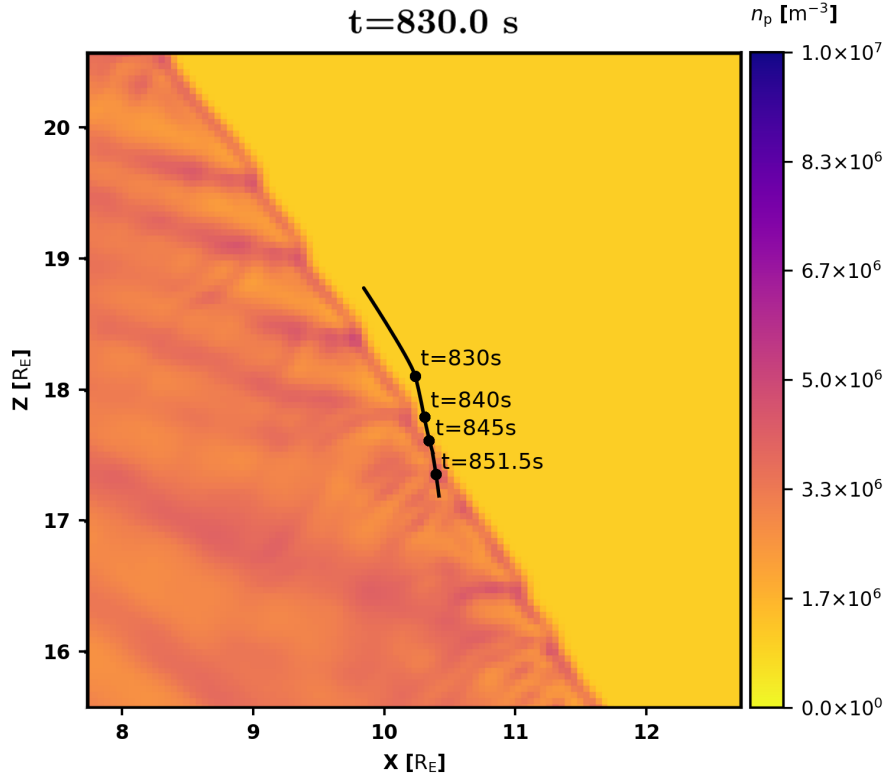


Figure 3.17: Trajectory estimate of the virtual spacecraft. The shock moves through a stationary point which forms a trajectory relative to the shock drawn in the figure. Relative position of the virtual spacecraft at four times are shown in the image. The colormap is of the shock when $t = 830$ s.

which is the furthest reflected ions travel from the shock as they gyrate back to the shock. This means the VDF is from the turning point region. The VDF is plotted in Figure 3.18. A reflected population is clearly visible in both of the panels as turquoise-green shape next to the solar wind population. From the theoretical velocity space image in the lower panel of Figure 1.3, we can see that in the turning point region only a single dot-like population would be present. The relatively small size of the "banana" in Figure 3.18 indicates that we indeed are near the turning point region. Only ions close or at the turning point are present in the reflected population in the VDF.

The reflected population fits the estimated first specular reflection curve well in both panels. There are less dense ions surrounding the reflected population. A second reflection population could be present further from the first reflection as the second reflection estimate is not far off from this population.

As we move forward in time we arrive to the second VDF at $t = 840$ s. In

$$t = 830 \text{ s}, x = 10.2R_E, z = 18.1R_E, \Delta n \approx 0.1R_E, \theta_{Bn} = 75.9^\circ$$

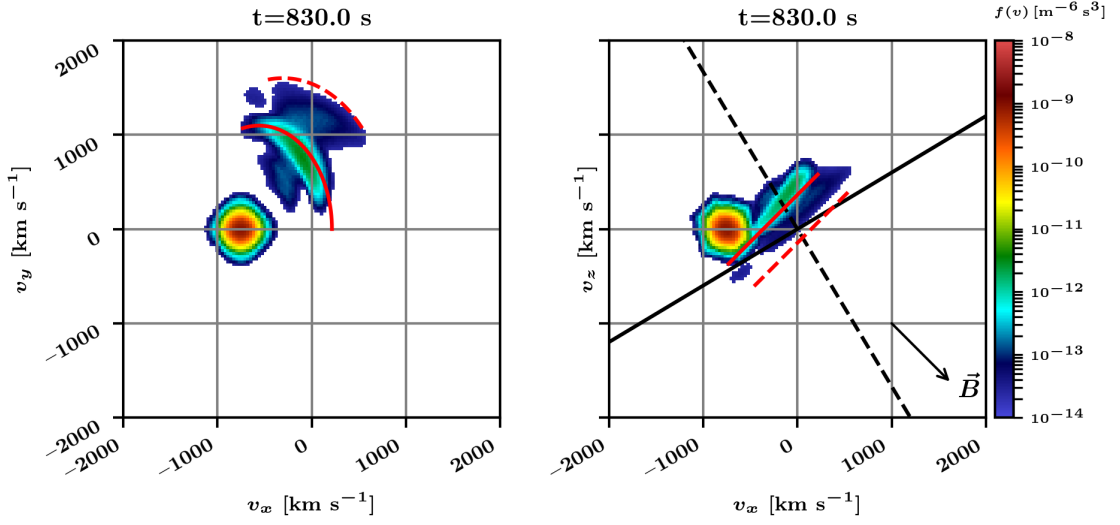


Figure 3.18: VDF of the quasi-perpendicular shock crossing when $t = 830$ s. Location of the VDF is panel a from Figure 3.16.

$$t = 840 \text{ s}, x = 10.2R_E, z = 18.1R_E, \Delta n \approx 0.1R_E, \theta_{Bn} = 75.8^\circ$$

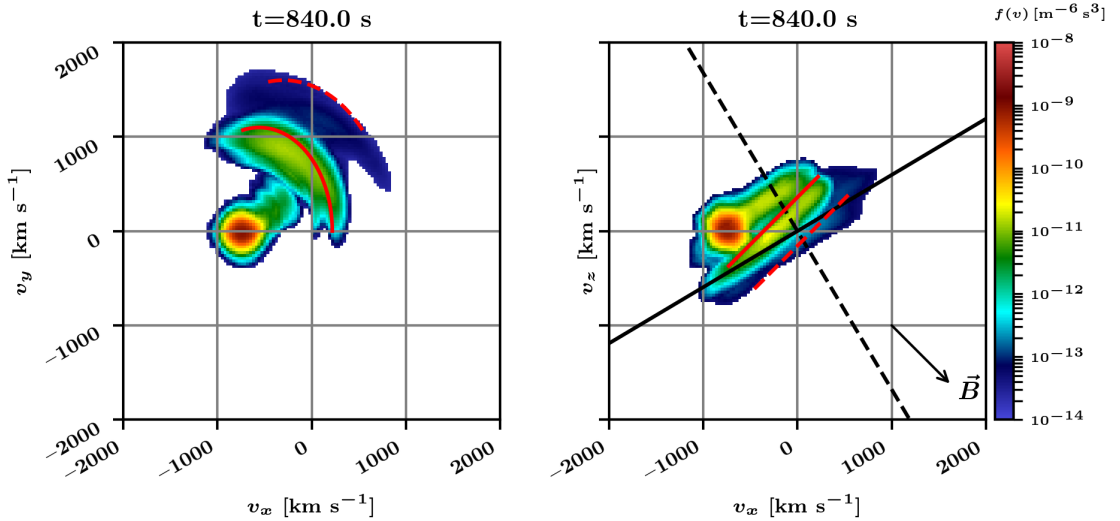


Figure 3.19: VDF of the quasi-perpendicular shock crossing when $t = 840$ s. Location of the VDF is panel b from Figure 3.16.

Figure 3.16b it can be seen that we are now close to the shock ramp. Instead of arriving head-on to the ramp the shock evolves in a way that the virtual spacecraft moves very close to a wave like structure, skimming the shock surface as the virtual spacecraft approaches the ramp.

In the VDF a clear reflected ion population is present in xy -plane, as seen in the

left panel of Figure 3.19. This VDF has previously been studied in Figure 3.10. The reflected ion population fits the estimation well in the perpendicular direction. A second reflection population is also present which fits the estimation well. The solar wind beam is extending towards the reflected population. The ions in the anomaly population have very low velocities in the normal direction. We speculate that these are ions, that did not get reflected gyrating in the downstream, temporarily crossing into upstream. In the parallel direction two populations are present with the solar wind population. As discussed previously, these are likely ions reflected off a different local shock geometry resulting in different velocities for specularly reflected ions.

$$t = 845 \text{ s}, x = 10.2R_E, z = 18.1R_E, \Delta n \approx 0.0R_E, \theta_{Bn} = 75.7^\circ$$

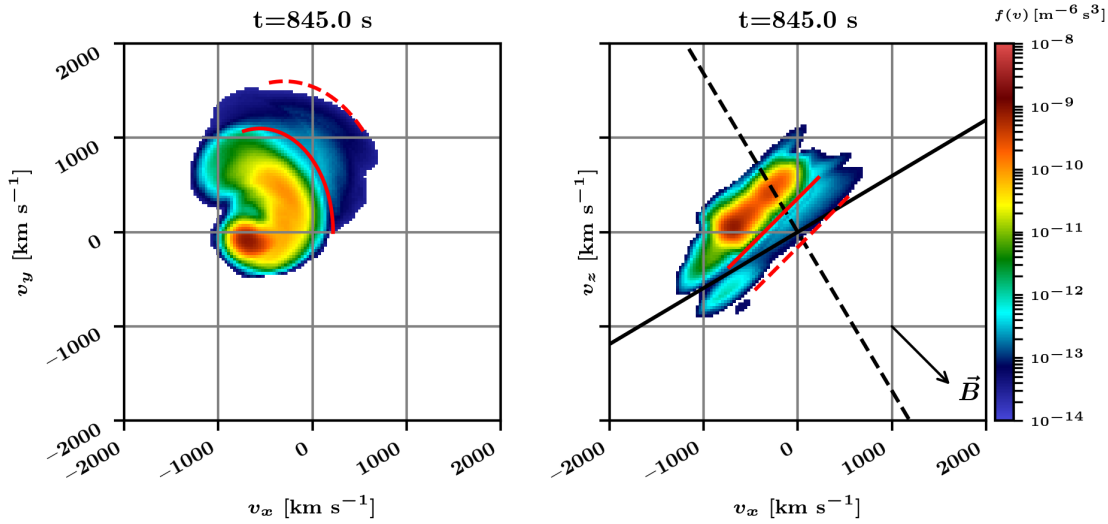


Figure 3.20: VDF of the quasi-perpendicular shock crossing when $t = 845$ s. Location of the VDF is panel c from Figure 3.16.

Moving forward, the virtual spacecraft is now at the shock ramp at $t = 845$ s. As the reflection is actively happening in the ramp the VDF looks very messy with the solar wind ions seemingly spreading to the reflected ion region from previous VDFs, see Figure 3.20. The VDF is now populated with upstream ions soon to be reflected, downstream ions that penetrated the shock, reflected ions, and ions being reflected from the shock. The specular reflection estimates do not show much correspondence with the populations as the ions are still undergoing reflection at the ramp.

Moving forward to $t = 851.5$ s the virtual spacecraft has now crossed the shock ramp and moved downstream. The VDF is a clear downstream population being just

$$t = 852 \text{ s}, x = 10.2R_E, z = 18.1R_E, \Delta n \approx 0.0R_E, \theta_{Bn} = 75.7^\circ$$

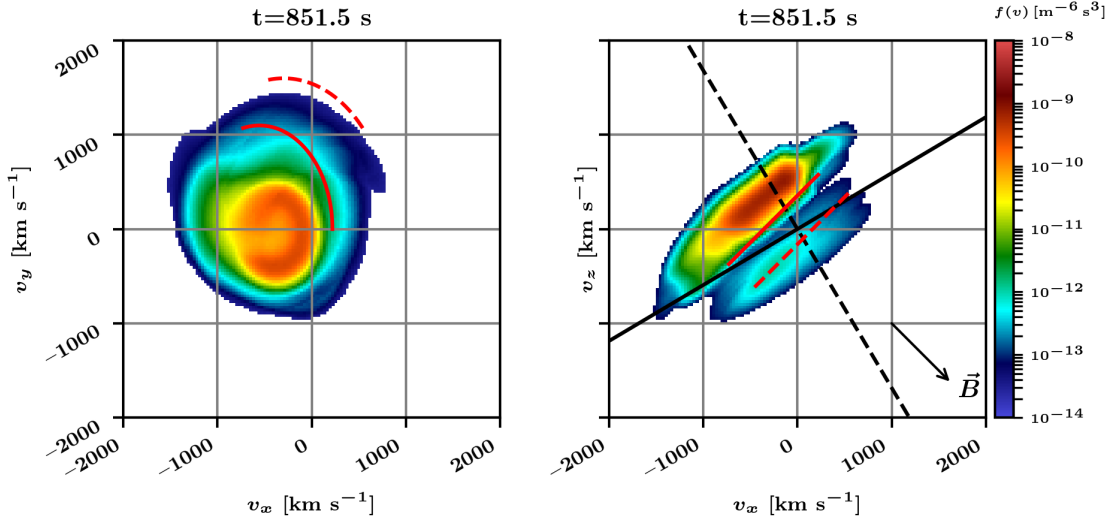


Figure 3.21: VDF of the quasi-perpendicular shock crossing when $t = 851.5$ s. Location of the VDF is panel d from Figure 3.16.

a single round population in the xy -plane, and an elliptical shape in xz -plane as seen in the left panel of Figure 3.21. In 3D this means the bulk population has a shape resembling a pancake. The gyration center of the bulk population has changed due to the plasma slowing down in the downstream and ions are now gyrating around the downstream flow velocity.

In the xz -plane, there is another significant population that fits the second reflection estimate well. The other population has gained parallel acceleration and is similar to one seen in previously in Figure 3.15. These ions may have gained the parallel acceleration via shock drift acceleration, where the ions gain velocity with every reflection from the shock. For θ_{Bn} between 60° and 70° , the ions can continue this process and gain enough energy to drift to the nose of the bow shock and escape upstream along the magnetic field forming a field aligned beam in the foreshock [Burgess et al., 2012].

4. Structure of the quasi-perpendicular bow shock

4.1 Bow shock cross section

A way to study the bow shock is to plot quantities from a simulated data across the shock in a single time step. This cross section of a bow shock is very similar in form to data from spacecraft observations but instead of time in the x-axis there is now distance. Here we will study cross section of the shock with three different times in a span of 20 seconds from a BCQ simulation. Location of the cross section in all three times is shown in Figure 4.1, where the blue line indicates the cross section. The location of the cross section is chosen around the same velocity cell, drawn here as a crosshair, used as the virtual spacecraft in Section 3.4.

Quantities from a cross section of a bow shock is plotted in Figure 4.2. The closest available velocity cell to the shock is shown as a blue vertical line. Though the different times vary quite much, a lot of common features between the three times can be seen, as expected. Upon hitting the shock the plasma is shocked and the magnetic field and number density both have a jump. This is the shock ramp located around the blue vertical line in Figure 4.2. There is a phase shift between the two where magnetic field is slightly ahead of the number density. The velocity drops as the solar wind speed slows down coming from the upstream to the downstream. The electric field has a more chaotic reaction to being shocked as the three times vary quite a lot from each other though there is a clear peak of $E_x \sim 1$ mV/m at the ramp. This is small compared to electric fields found in nature [Walker et al., 2004].

After the ramp a more turbulent downstream region begins where the the values behave according to different wave modes. Very clear undershoot and overshoot regions are present. When comparing the magnetic field to the density, we can see that the waves seem to mirror each other; when the magnetic field wave is at a local

maximum the number density is at a local minimum. This indicates that mirror mode waves are present in the shock [Hoilijoki et al., 2016].

The movement of the shock can be seen in all four panels as the three times are distinctly seen in each one. The major features of the shock are present in each time step, but local features are different through the different times. This means the local features of the shock evolve in a timescale less than 10 s.

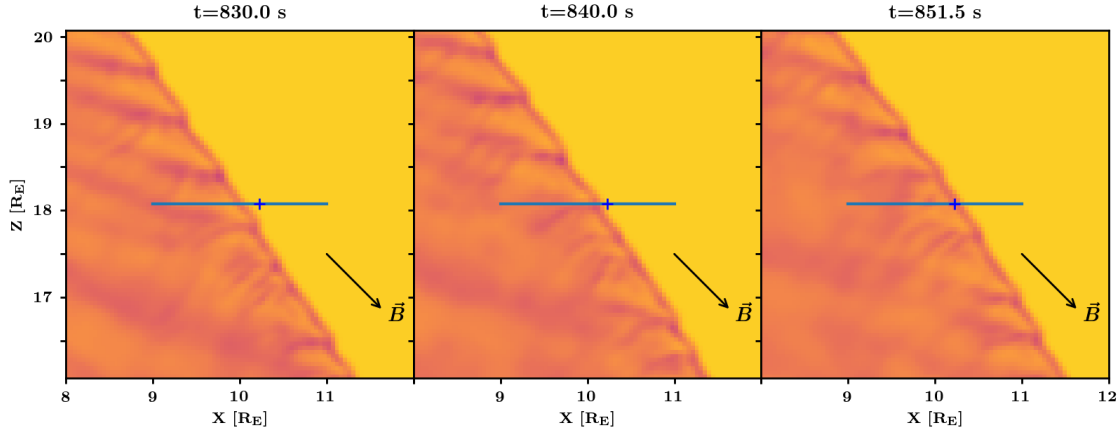


Figure 4.1: Colormaps of the bow shock at three times used in Figure 4.2 with a location of the cross section drawn as a blue line. The nearest velocity cell is drawn as blue crosshair. Direction of the upstream magnetic field is drawn as an arrow.

4.2 Virtual spacecraft

Another way to analyze simulated data of a bow shock is by choosing coordinates in a single spot and then taking enough time steps for the shock to move across the chosen coordinates. This virtual spacecraft method was previously used in Section 3.4 of this thesis. Here we will analyze the properties of the shock using the same virtual spacecraft as before.

Data from virtual spacecraft crossing the bow shock is shown in Figure 4.3. Here the shock crossing is seen as a time series where it takes around 30 seconds for the spacecraft to move fully from upstream to downstream. In the simulation, the shock is moving towards the Sun with a velocity of $V_{sh} \approx 50 \text{ km s}^{-1}$. This means the shock crossing is about $\sim 1500 \text{ km} \approx 0.235 R_E$ long in length which is around the size of the shock ramp and its surroundings in the cross section seen in Figure 4.2. In the virtual spacecraft data, the shock crossing appears to take longer, however this is only due to scaling of the x-axis. Even though the shock crossing is similar in both methods it is apparent that the virtual spacecraft has a better resolution

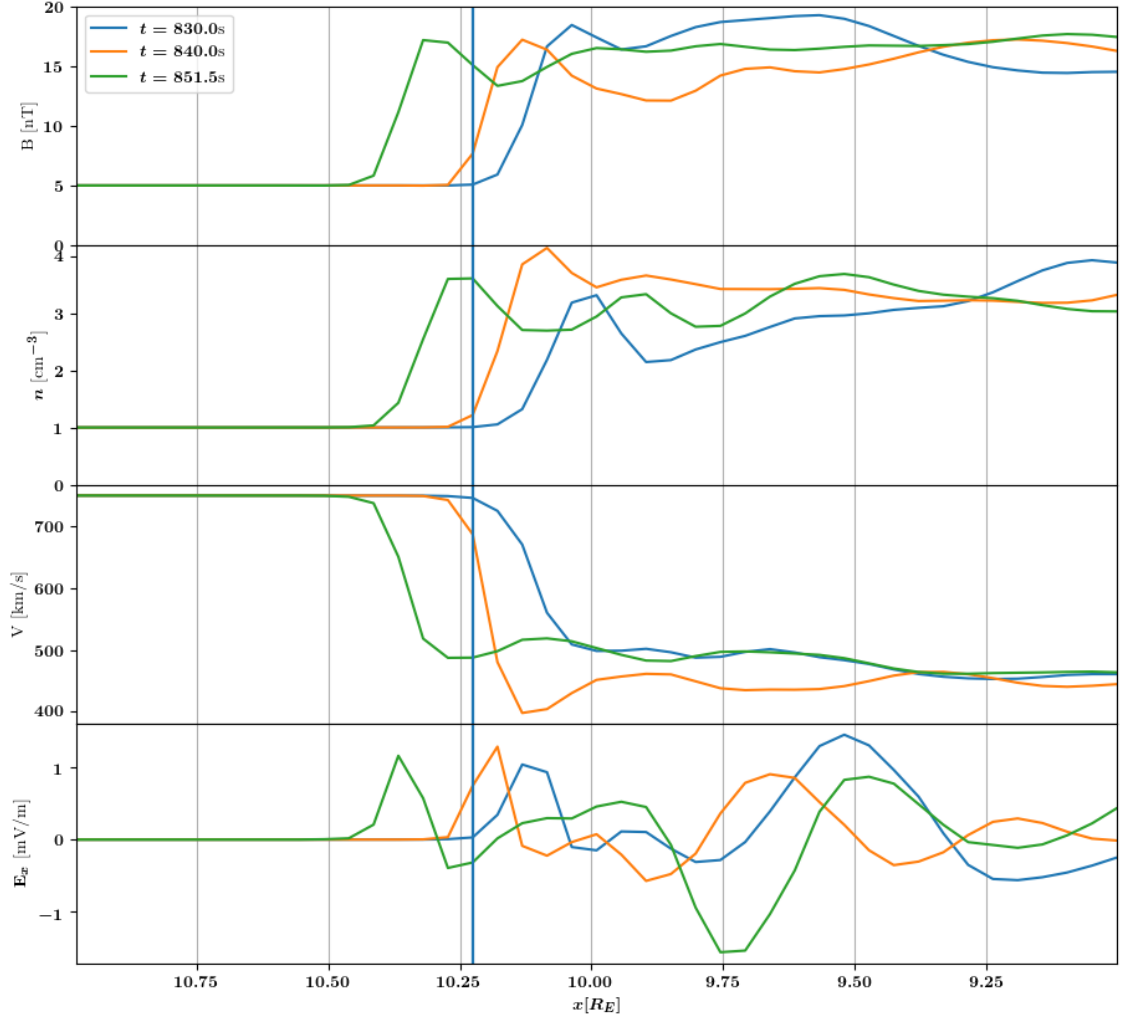


Figure 4.2: Cross section of the quasi-perpendicular bow shock from three times. Plotted quantities are the magnetic field, number density, velocity and the x -component of the electric field. The closest velocity cell is drawn as a vertical blue line.

compared to the shock cross section.

Looking from the upstream, the shock looks very much like expected with clear foot and a ramp visible. After the shock ramp there is a possible overshoot region. The overshoot region does not have such a clear shape as in the cross section but instead has three separate peaks seen in Figure 4.3b. The peaks are seen as wave-like structure in magnetic field with the first one being clearly larger than the other two. This can bring up uncertainty whether the overshoot is the three peaks combined or just the first one. After the overshoot, there is an undershoot region which ends abruptly as the number density rises again. This could be a mirror-mode wave as the magnetic field decreases at the same time as the number density starts to increase. The overall shape of the number density is similar to the $t = 851.5\text{ s}$ curve

of the shock cross section with both having overshoot, undershoot and then another increase in density. The velocity drops expectedly as the solar wind is shocked and slowed down. The electric field components are shown in Figure 4.3d including the electric field component along the shock normal vector E_n . As expected E_x and E_n are very similar in shape though at the shock ramp E_n has a higher peak.

The forces acting on an ion are different depending whether they act along or perpendicular to \mathbf{B} . This causes the temperature T to have different distributions parallel T_{\parallel} and perpendicular T_{\perp} to the magnetic field. Reflected ions produce highly anisotropic temperature distributions [Winske and Quest, 1988]. This temperature anisotropy can be seen in Figure 4.3d, where T_{\perp} starts to rise at the very beginning of the shock foot, whereas T_{\parallel} stays relatively low during the whole crossing. The anisotropy ratio $T_{\perp}/T_{\parallel} \approx 15$. In nature, the anisotropy ratio is about order of magnitude smaller [Johlander et al., 2018]. The high T_{\perp}/T_{\parallel} is common in the shock in Vlasiator [Dubart et al., 2020].

4.3 Shock potential

One advantage of the virtual spacecraft is that it provides the VDF through the shock. This makes it possible to calculate quantities that are impossible to measure from the cross section of the shock. The electric field (seen in Figure 4.3c) plays an important role in the plasma dynamics in the shock. While the electric field can simply be measured from the cross section, the same is not possible for the cross-shock potential as it requires the spatial integration of the electric field across the shock. The work done on to move a charge q from a to b is

$$W = \int_a^b \mathbf{F} \cdot d\mathbf{l} = -q \int_a^b \mathbf{E} \cdot d\mathbf{l} = q[\Phi(\mathbf{b}) - \Phi(\mathbf{a})], \quad (4.1)$$

where Φ is the electric potential [Griffiths, 1999]. Much like measuring altitude, the choice of the origin point a is important as the choice of origin directly affects the calculated potential. A common convention is that the electric potential upstream of the shock is 0. This way we can calculate change in the electric potential through the shock. We will use the name shock potential Φ for this value from now on.

Since Vlasiator uses a cartesian grid to save quantities, it is convenient to assume that the path to integrate is along x and therefore integrate the line integral over E_x . It would be more cumbersome to integrate along $\hat{\mathbf{n}}$ to get the normal incidence potential [Dimmock et al., 2011], since the cells needed for the integral

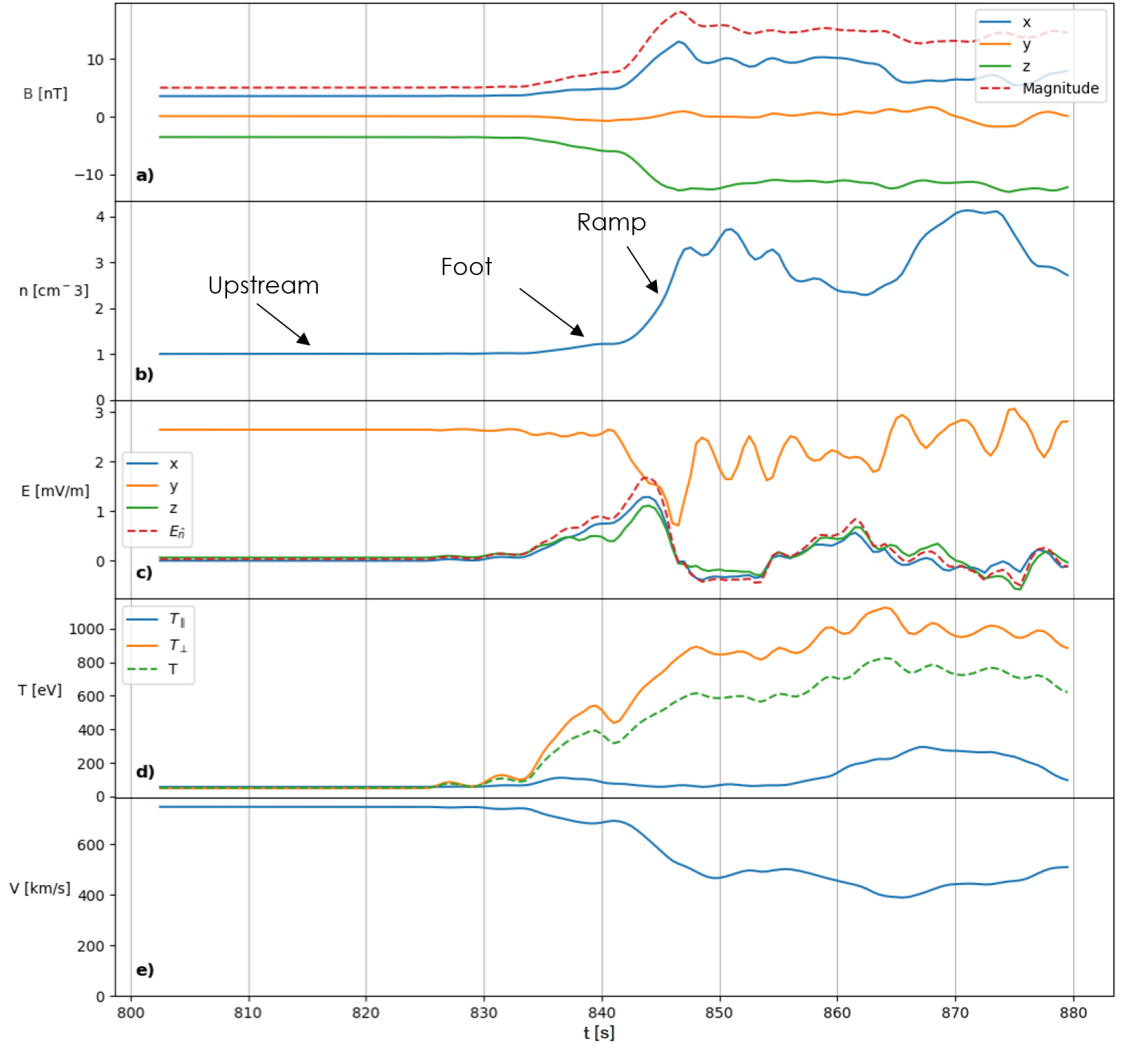


Figure 4.3: Virtual spacecraft quasi-perpendicular bow shock crossing. Quantities plotted are the magnetic field, number density, electric field, temperature and velocity. Distinct features of the shock are annotated with number density.

would have to be calculated. Integrating E_x is a decent assumption because the solar wind is along x . In the downstream, this assumption is not as accurate, as direction of the ions changes as they hit the shock. In the shock, the electric field is slightly along z -axis, which may cause a slight error when integrating only E_x , but this error is small. The shock potential is calculated as

$$\Phi(x) = - \int_{x+L}^x E_x dr, \quad (4.2)$$

where x is the location of the virtual spacecraft and L is a distance sufficient to

reach upstream. In practice, the integral is calculated for every timestep as

$$\Phi(x) = \sum_{i=0}^{99} E_{xi} \Delta r, \quad (4.3)$$

where E_{xi} is the electric field at i th cell towards the Sun from the position of the virtual spacecraft and Δr is the size of one cell $\Delta r = 300$ km. The 100 cells is an arbitrarily chosen number large enough to reach clearly to the upstream. The potential at the shock has a peak of $\Phi(x) = 800$ V at the shock (Figure 4.4d). This is $\sim 30\%$ of the upstream kinetic energy which is in good agreement to observations [Dimmock et al., 2012].

Using equation (4.3) for shocks in space that are measured by spacecraft is not realistic as it requires simultaneous observations from 100 spacecraft in a straight line. Since this is not reasonable, another method is needed to calculate the shock potential as a spacecraft would "see" it using only data from one cell. This is how potential is measured in practice [Dimmock et al., 2012]. Instead of using x as the spatial coordinate to integrate over, we will now use time t

$$\Phi(t) = - \int_{t_0}^{t_n} E_x V_{sh} dt, \quad (4.4)$$

where $V_{sh} = 50 \text{ km s}^{-1}$ is the shock speed, t_0 is the time at the start of the observations in upstream and t_n is the latest observation. The integration is performed again with a sum

$$\Phi(t) = \sum_{i=0}^n E_{xi} V_{sh} \Delta t, \quad (4.5)$$

where n is the number of the newest observation and Δt is the length of one timestep $\Delta t = 0.5$ s. The shock potential calculated with time follows $\Phi(x)$ but is smoothed to a degree where the peak value at the shock is $\Phi(t) \approx 400$ V as seen in Figure 4.4d. This is $\sim 15\%$ of the upstream kinetic energy. Although this method emulates real spacecraft observations, the actual observations by Dimmock et al. [2012] are more in line with $\Phi(x)$ as there is a peak in number of shocks observed with $\sim 30\%$ upstream kinetic energy. This shows that the spacecraft technique to measure Φ can be somewhat unreliable.

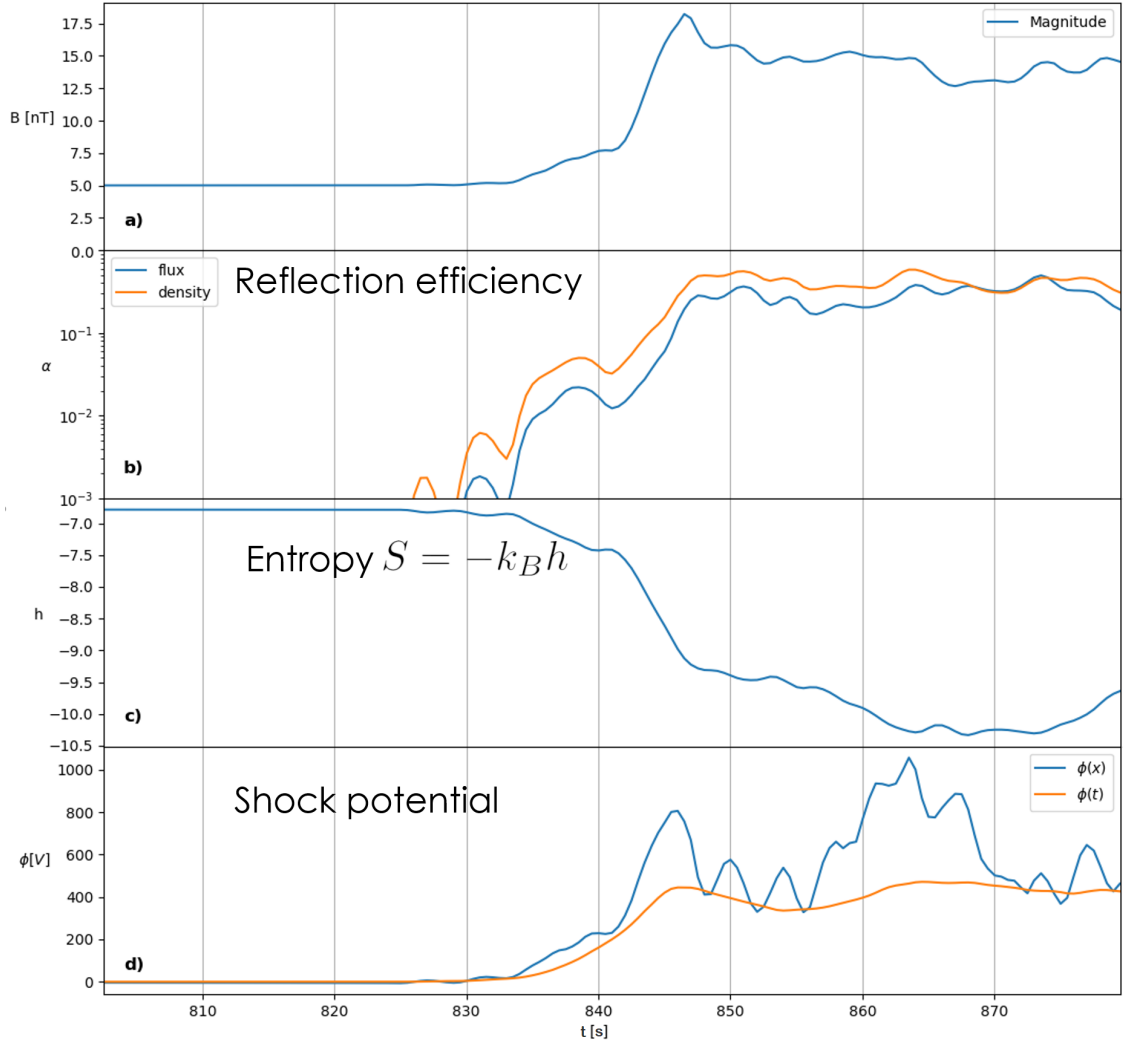


Figure 4.4: Virtual spacecraft quasi-perpendicular bow shock crossing. Quantities plotted are the magnitude of the magnetic field, reflection efficiency, h parameter of the entropy and shock potential. Magnetic field is plotted for easy comparison to the shock profile.

4.4 Ion dynamics at the shock

As the solar wind ions hit the quasi-perpendicular bow shock, a portion of them are reflected back upstream. Previously we have studied ion reflection in a more qualitative sense and found that ion reflection is nearly specular in nature. Now we will look at more quantitative aspects of ion reflection at the shock. A fundamental quantity is how large of a portion of the ions are reflected. This so called reflection efficiency plays a major role in shock dynamics. The behaviour of reflected ions was previously introduced and studied in Chapter 3, but the portion of the reflected ions is yet to be investigated.

The percentage of the ions that are reflected can be calculated as the flux of ions with a positive v_n divided by the solar wind flux, as by Leroy et al. [1982]. We can get the flux by using the first order moment of the velocity distribution function [Paschmann et al., 1998]. Using this, we get

$$\alpha = \frac{\sum_{v_n > 0} f v_n (\Delta v)^3}{n_{sw} \mathbf{V}_{sw} \cdot \hat{\mathbf{n}}}, \quad (4.6)$$

where f is the velocity distribution function, v_n is the velocity of the ion in the direction of $\hat{\mathbf{n}}$, Δv is the size of a velocity cell, n_{sw} is the solar wind density and \mathbf{V}_{sw} is the solar wind velocity. Only cells with $v_n > 0$ are calculated in the flux to get the flux of the reflected ions.

Another way to estimate reflection efficiency is by calculating and comparing the densities of the two ion populations, as in [Sckopke et al., 1983]. Density can be calculating using the zeroth moment of the velocity distribution function [Paschmann et al., 1998]. The percentage can be calculated by dividing the density of reflected ions with the incident ions

$$\alpha' = \frac{\sum_{v_n > 0} f(\Delta v)^3}{\sum_{v_n < 0} f(\Delta v)^3}. \quad (4.7)$$

In practice, the difference between equations (4.6) and (4.7) is that α is the probability of an ion being reflected compared to α' which is the fraction of reflected ions.

Ion reflection efficiency calculated using both the flux α and density α' is shown in Figure 4.4b in logarithmic scale. Both flux and density have similar shape across the shock with α' being slightly higher throughout the shock except in the downstream region. The reflection efficiency has a first noticeable bump in the foot of the shock, after which it has a slight decrease before rising sharply at the shock. The reflection efficiency reaches its maximum at the shock a few seconds after the potential and magnetic field maximum. In the downstream the reflection efficiency stays around the same with α varying around ~ 0.4 and $\alpha' \approx 0.3$. Leroy et al. [1982] and Sckopke et al. [1983] measured the reflection efficiency at the peak of the shock potential. In Figure 4.4, this is at $t = 846$ s. Here the values are $\alpha \approx 0.12$ and $\alpha' \approx 0.28$. In simulations, Leroy et al. [1982] found that the average value for $\alpha = 0.137$ and Sckopke et al. [1983] measured $\alpha' \sim 0.15 - 0.25$ with spacecraft observations. Our results are in good agreement with literature showing

that ion reflection efficiency in Vlasiator is in quantitative agreement with previous simulations and spacecraft observations.

Entropy generation through the bow shock has been studied with spacecraft data by Parks et al. [2012] and with simulations by Yang et al. [2014]. The entropy is measured as h parameter in the Gibbs entropy $S_g = -k_B h$

$$h = \sum_i p_i \ln p_i, \quad (4.8)$$

where

$$p_i = f_i \Delta v^3 / n \quad (4.9)$$

is the probability of an ion being in a certain velocity cell. The h parameter is calculated in Figure 4.4c. The h starts around ~ -7 and starts to decrease at the shock foot. At the shock ramp the h starts to decrease faster. After the ramp, h continues to decrease but slower. As the h is negative the entropy increases through the shock. Since collisions are not modeled in the Vlasiator simulations, the entropy is expected to remain unchanged through the shock as entropy is preserved without collisions [Mouhot and Villani, 2011]. Despite this, our results are very similar to those found by Parks et al. [2012], where the h changed by ~ -2 , compared to $\Delta h \sim -3$ in our work. It is reasonable to assume that the extra entropy generation in Vlasiator is numerical in nature.

All in all ion dynamics in Vlasiator are in line with observations and previous simulations.

5. Discussion and conclusions

In this project, we have studied the ion reflection at the Earth's quasi-perpendicular bow shock. Using two Vlasiator simulations we investigated velocity distribution functions (VDF) to see how ions behave at different parts of the quasi-perpendicular shock. We also simulated what a spacecraft would see crossing the bow shock. This virtual spacecraft (VSC) was used to study the evolution of a VDF during a quasi-perpendicular shock crossing. Finally we used a cross section of the bow shock at a single point in time, and the data from the VSC shock crossing to study properties such as magnetic field, density, reflection efficiency and cross-shock potential. Ion dynamics, such as reflection efficiency, was also investigated using the VSC data.

We derived expressions (equation 3.19) for velocities of ions specularly reflected from the bow shock in the normal incidence frame. These expressions were transformed into the simulation frame to estimate specular reflection as curve where a reflected ion population is expected to be. Since the expressions are dependent on the shock normal vector $\hat{\mathbf{n}}$, a method for determining $\hat{\mathbf{n}}$ was created and used to estimate specular reflection at an arbitrary point on the bow shock. We investigated four kinds of reflection: a specular reflection in the normal incidence frame, a specular reflection from a surface moving with the downstream flow speed, a specular reflection from a surface moving with half of the downstream flow speed and a specular reflection from a surface moving with the electron flow. We found that all estimates were in good agreement with the observed ion VDFs, which means ions are nearly specularly reflected. The best estimate varied, but often the reflected population was most accurately estimated by the "intermediate frame" reflection. We conclude that ions are nearly specularly reflected off the shock in Vlasiator in a frame moving with half the downstream flow speed.

In many VDFs we found evidence of ions being reflected off the shock twice, which can be important for ion acceleration [e.g. Caprioli et al., 2015]. To study this, we expanded our method so it can estimate more than one specular reflections. We investigated the number of possible reflections depending on the angle θ_{Bn} . We

found that in the frame moving with downstream flow speed only two reflections are ever possible, because the ion loses energy as it is reflected from a moving surface. A reflected ion does not gain enough velocity to turn away from the shock and escapes downstream. We used the method to study the populations of ions reflected twice. We found that the model was in good agreement with the observed populations in the normal incidence frame or the intermediate frame, depending on the VDF. We also found that the reflection estimates were accurate in the direction perpendicular to \mathbf{B} , but in the parallel direction the model tended to overestimate the speed of the reflected ions.

In Vlasiator the shock moves away from Earth with time which means a single velocity cell can act as a virtual spacecraft that crosses the shock. We used this to study how a VDF evolves crossing the shock. We used the intermediate frame estimations for two specular reflections to study reflected populations. We found that upstream of the shock, the reflection estimates were accurate in the direction perpendicular to the magnetic field. In the parallel direction, two reflected populations became apparent as the VSC moved closer to the shock. This is likely caused by incoming ions being reflected off the shock with vastly different $\hat{\mathbf{n}}$ due to local geometry. Downstream of the shock we found a population which had gained significant parallel acceleration, possibly gained from shock drift acceleration. The most energetic of these ions could potentially gain enough energy to drift to and escape from the nose of the shock.

We used a cross section at three different times to study the properties and evolution of the shock. The results showed clear features expected from a quasi-perpendicular bow shock including undershoot and overshoot regions. Downstream of the shock, the magnetic field and number density showed features that indicated the presence of mirror mode waves. The movement of the shock was clearly visible comparing major features of the shock in each time, however the small scale features were different in each time meaning the shock evolves on timescales less than 10 s. To further analyze the structure, we used the VSC data to study the properties of the shock in a similar way. Again, the major features expected in a bow shock were present but here the undershoot and overshoot regions were not as clear. A high temperature anisotropy $T_{\perp}/T_{\parallel} \approx 15$ was found in the VSC data. This is order of magnitude larger than anisotropy found in nature. The high temperature anisotropy of the shock has been observed before in Vlasiator and could be due to the spatial resolution used in the simulations [Dubart et al., 2020].

An advantage in using VSC to study the structure of a bow shock is that it

provides a VDF through the shock, which makes it possible to study quantities that cannot be measured from a cross section. We used the VSC to study the cross-shock potential Φ in two ways: integrating over distance x (the "real" potential), and over time t , which is what a spacecraft would observe. We found that at the peak of the shock $\Phi(x) \approx 800$ V and $\Phi(t) \approx 400$ V, which is 30% and 15% of the upstream ion kinetic energy, respectively. $\Phi(t)$ appears similar in shape as $\Phi(x)$ but with a more smooth profile. Since spacecraft can only measure $\Phi(t)$, this means spacecraft observations may have quite large uncertainties. Although, observations [Dimmock et al., 2012] match $\Phi(x)$ very well. The VSC was also used to study ion reflection efficiency α at the shock in two ways: the flux of the reflected ions ($v_n > 0$) divided by the solar wind flux [Leroy et al., 1982], and the density of the reflected ion population compared to incident density [Sckopke et al., 1983]. We found that in both cases α is in good agreement with the observed values. Lastly, we calculated entropy across the shock. The results were again a good match with observations [Parks et al., 2012]. However, since the collisions are not modeled in Vlasiator, the entropy is expected to remain unchanged and the entropy observed in Vlasiator is of numerical origin.

The results of this thesis have showed that ion reflection in the quasi-perpendicular bow shock in Vlasiator is in quantitative agreement with observations. The reflected ions fit our models of specular reflection well. In future work, the specular reflection estimation model could be fitted with a more accurate model of the shock geometry, providing $\hat{\mathbf{n}}$ that matches the local geometry of the shock better. The methods developed here could be used to study acceleration mechanisms and the formation of the field aligned beam. The analysis used here could also be applied to finer resolution simulation runs, since the resolution affects the properties of the shock, and newer simulation runs that have the electron pressure term added to the Ohm's law. Additionally the analysis could be performed on 3D simulation runs. The comparison of reflection in the different frames could be studied in other simulations or with spacecraft observations.

Our results with current Vlasiator simulations have already been in good line with spacecraft observations. In the future, as Vlasiator is developed to be more and more accurate it can help further our understanding of ion reflection and acceleration in shocks.

Acknowledgements

The author acknowledges the European Research Council for Starting grant 200141-QuESpace, with which Vlasiator was developed, and Consolidator grant Consolidator grant 682068-PRESTISSIMO awarded to further develop Vlasiator and use it for scientific investigations. Also acknowledged is the Academy of Finland for grant number 312351, which funds The Finnish Centre of Excellence in Research of Sustainable Space, which participates in supporting Vlasiator development and science. The author wishes to thank the Finnish Grid and Cloud Infrastructure (FGCI) and specifically the University of Helsinki computing services for supporting this project with computational and data storage resources.

I would like to thank my adviser Andreas Johlander for valuable discussions and helpful inputs, and censors of this thesis prof. Minna Palmroth and Dr. Markus Battarbee for their part. I would also like to thank my friends and family for their support and continuous encouragement.

Bibliography

- A. Balogh and R. Treumann. *Physics of Collisionless Shocks: Space Plasma Shock Waves*. ISSI Scientific Report Series. Springer New York, 2013. ISBN 9781461460992. URL https://books.google.fi/books?id=mR4_AAAAQBAJ.
- M. Battarbee, U. Ganse, Y. Pfau-Kempf, L. Turc, T. Brito, M. Grandin, T. Koskela, and M. Palmroth. Non-locality of earth’s quasi-parallel bow shock: injection of thermal protons in a hybrid-vlasov simulation. *Annales Geophysicae*, 38(3):625–643, 2020. doi: 10.5194/angeo-38-625-2020. URL <https://angeo.copernicus.org/articles/38/625/2020/>.
- M. Battarbee, T. Brito, M. Alho, Y. Pfau-Kempf, M. Grandin, U. Ganse, K. Papadakis, A. Johlander, L. Turc, M. Dubart, and M. Palmroth. Vlasov simulation of electrons in the context of hybrid global models: an evlasiator approach. *Annales Geophysicae*, 39(1):85–103, 2021. doi: 10.5194/angeo-39-85-2021. URL <https://angeo.copernicus.org/articles/39/85/2021/>.
- R. D. Blandford and J. P. Ostriker. Particle acceleration by astrophysical shocks. *Astrophysical Journal Letters*, 221:L29–L32, Apr. 1978. doi: 10.1086/182658.
- D. Burgess, E. Möbius, and M. Scholer. Ion Acceleration at the Earth’s Bow Shock. *Space Sci. Rev.*, 173(1-4):5–47, Nov. 2012. doi: 10.1007/s11214-012-9901-5.
- I. H. Cairns and J. G. Lyon. MHD simulations of Earth’s bow shock at low Mach numbers: Standoff distances. *J. Geophys. Res.*, 100(A9):17173–17180, Sept. 1995. doi: 10.1029/95JA00993.
- D. Caprioli, A.-R. Pop, and A. Spitkovsky. Simulations and Theory of Ion Injection at Non-relativistic Collisionless Shocks. *Astrophysical Journal Letters*, 798(2): L28, Jan. 2015. doi: 10.1088/2041-8205/798/2/L28.
- F. F. Chen. *Introduction to Plasma Physics and Controlled Fusion*. Springer, Cham, 2016. doi: 10.1007/978-3-319-22309-4.

- A. P. Dimmock, M. A. Balikhin, and Y. Hobara. Comparison of three methods for the estimation of cross-shock electric potential using cluster data. *Annales Geophysicae*, 29(5):815–822, 2011. doi: 10.5194/angeo-29-815-2011. URL <https://angeo.copernicus.org/articles/29/815/2011/>.
- A. P. Dimmock, M. A. Balikhin, V. V. Krasnoselskikh, S. N. Walker, S. D. Bale, and Y. Hobara. A statistical study of the cross-shock electric potential at low Mach number, quasi-perpendicular bow shock crossings using Cluster data. *Journal of Geophysical Research (Space Physics)*, 117(A2):A02210, Feb. 2012. doi: 10.1029/2011JA017089.
- M. Dubart, U. Ganse, A. Osmane, A. Johlander, M. Battarbee, M. Grandin, Y. Pfau-Kempf, L. Turc, and M. Palmroth. Resolution dependence of magnetosheath waves in global hybrid-Vlasov simulations. *Annales Geophysicae*, 38(6):1283–1298, Dec. 2020. doi: 10.5194/angeo-38-1283-2020.
- J. P. Edmiston and C. F. Kennel. A parametric survey of the first critical Mach number for a fast MHD shock. *Journal of Plasma Physics*, 32(3):429–441, Dec. 1984. doi: 10.1017/S002237780000218X.
- D. H. Fairfield. Average and unusual locations of the Earth’s magnetopause and bow shock. *J. Geophys. Res.*, 76(28):6700, Jan. 1971. doi: 10.1029/JA076i028p06700.
- M. H. Farris, S. M. Petrinec, and C. T. Russell. The thickness of the magnetosheath: Constraints on the polytropic index. *Geophys. Res. Lett.*, 18(10):1821–1824, Oct. 1991. doi: 10.1029/91GL02090.
- V. Formisano, P. C. Hedgecock, G. Moreno, F. Palmiotto, and J. K. Chao. Solar wind interaction with the Earth’s magnetic field: 2. Magnetohydrodynamic bow shock. *J. Geophys. Res.*, 78(19):3731, Jan. 1973. doi: 10.1029/JA078i019p03731.
- J. Geiss, G. Gloeckler, and R. von Steiger. Origin of the Solar Wind From Composition Data. *Space Sci. Rev.*, 72(1-2):49–60, Apr. 1995. doi: 10.1007/BF00768753.
- D. J. Griffiths. *Introduction to electrodynamics*. Prentice Hall, Upper Saddle River (NJ), 3rd ed. edition, 1999. ISBN 0-13-919960-8.
- S. Hoilijoki, M. Palmroth, B. M. Walsh, Y. Pfau-Kempf, S. von Alfthan, U. Ganse, O. Hannuksela, and R. Vainio. Mirror modes in the Earth’s magnetosheath: Results from a global hybrid-Vlasov simulation. *Journal of Geophysical Research (Space Physics)*, 121(5):4191–4204, May 2016. doi: 10.1002/2015JA022026.

- A. Johlander. *Ion dynamics and structure of collisionless shocks in space*. PhD thesis, Uppsala University, Space Plasma Physics, Swedish Institute of Space Physics, Uppsala Division, 2019.
- A. Johlander, S. J. Schwartz, A. Vaivads, Y. V. Khotyaintsev, I. Gingell, I. B. Peng, S. Markidis, P. A. Lindqvist, R. E. Ergun, G. T. Marklund, F. Plaschke, W. Magnes, R. J. Strangeway, C. T. Russell, H. Wei, R. B. Torbert, W. R. Paterson, D. J. Gershman, J. C. Dorelli, L. A. Avanov, B. Lavraud, Y. Saito, B. L. Giles, C. J. Pollock, and J. L. Burch. Rippled Quasiperpendicular Shock Observed by the Magnetospheric Multiscale Spacecraft. *Phys. Rev. Lett.*, 117(16):165101, Oct. 2016. doi: 10.1103/PhysRevLett.117.165101.
- A. Johlander, A. Vaivads, Y. V. Khotyaintsev, I. Gingell, S. J. Schwartz, B. L. Giles, R. B. Torbert, and C. T. Russell. Shock ripples observed by the MMS spacecraft: ion reflection and dispersive properties. *Plasma Physics and Controlled Fusion*, 60(12):125006, Dec. 2018. doi: 10.1088/1361-6587/aae920.
- Y. Kempf, D. Pokhotelov, O. Gutynska, L. B. Wilson III, B. M. Walsh, S. v. Alfthan, O. Hannuksela, D. G. Sibeck, and M. Palmroth. Ion distributions in the earth's foreshock: Hybrid-vlasov simulation and themis observations. *Journal of Geophysical Research: Space Physics*, 120(5):3684–3701, 2015. doi: <https://doi.org/10.1002/2014JA020519>. URL <https://agupubs.onlinelibrary.wiley.com/doi/abs/10.1002/2014JA020519>.
- C. F. Kennel. Critical Mach numbers in classical magnetohydrodynamics. *J. Geophys. Res.*, 92(A12):13427–13437, Dec. 1987. doi: 10.1029/JA092iA12p13427.
- B.-C. Koo and C. Park. *Supernova Remnant Cassiopeia A*, pages 161–178. Springer International Publishing, Cham, 2017. ISBN 978-3-319-21846-5. doi: 10.1007/978-3-319-21846-5_50. URL https://doi.org/10.1007/978-3-319-21846-5_50.
- K. Koyama, R. Petre, E. V. Gotthelf, U. Hwang, M. Matsuura, M. Ozaki, and S. S. Holt. Evidence for shock acceleration of high-energy electrons in the supernova remnant SN1006. *Nature*, 378(6554):255–258, Nov. 1995. doi: 10.1038/378255a0.
- M. M. Leroy, D. Winske, C. C. Goodrich, C. S. Wu, and K. Papadopoulos. The structure of perpendicular bow shocks. *J. Geophys. Res.*, 87(A7):5081–5094, July 1982. doi: 10.1029/JA087iA07p05081.

- G. Morlino and D. Caprioli. Strong evidence for hadron acceleration in Tycho's supernova remnant. *A&A*, 538:A81, Feb. 2012. doi: 10.1051/0004-6361/201117855.
- C. Mouhot and C. Villani. On Landau damping. *Acta Mathematica*, 207(1):29 – 201, 2011. doi: 10.1007/s11511-011-0068-9. URL <https://doi.org/10.1007/s11511-011-0068-9>.
- M. Palmroth, U. Ganse, Y. Pfau-Kempf, M. Battarbee, L. Turc, T. Brito, M. Grandin, S. Hoilijoki, A. Sandroos, and S. von Alfthan. Vlasov methods in space physics and astrophysics. *Living Reviews in Computational Astrophysics*, 4(1):1, Aug. 2018. doi: 10.1007/s41115-018-0003-2.
- E. N. Parker. Dynamics of the Interplanetary Gas and Magnetic Fields. *ApJ*, 128: 664, Nov. 1958. doi: 10.1086/146579.
- G. K. Parks, E. Lee, M. McCarthy, M. Goldstein, S. Y. Fu, J. B. Cao, P. Canu, N. Lin, M. Wilber, I. Dandouras, H. Réme, and A. Fazakerley. Entropy generation across earth's collisionless bow shock. *Phys. Rev. Lett.*, 108:061102, Feb 2012. doi: 10.1103/PhysRevLett.108.061102. URL <https://link.aps.org/doi/10.1103/PhysRevLett.108.061102>.
- G. Paschmann, A. N. Fazakerley, and S. J. Schwartz. Moments of Plasma Velocity Distributions. *ISSI Scientific Reports Series*, 1:125–158, Jan. 1998.
- G. Paschmann, S. J. Schwartz, C. P. Escoubet, and S. Haaland. *Outer Magnetospheric Boundaries: Cluster Results*. Springer, Dordrecht, 2005. doi: 10.1007/1-4020-4582-4.
- Y. Pfau-Kempf. *Vlasiator: From local to global magnetospheric hybrid-Vlasov simulations*. PhD thesis, University of Helsinki, Finland, Jan. 2016. URL <http://hdl.handle.net/10138/175914>.
- A. J. Ridley, T. I. Gombosi, I. V. Sokolov, G. Tóth, and D. T. Welling. Numerical considerations in simulating the global magnetosphere. *Annales Geophysicae*, 28 (8):1589–1614, 2010. doi: 10.5194/angeo-28-1589-2010. URL <https://angeo.copernicus.org/articles/28/1589/2010/>.
- S. J. Schwartz. Shock and Discontinuity Normals, Mach Numbers, and Related Parameters. *ISSI Scientific Reports Series*, 1:249–270, 1998.

- S. J. Schwartz, M. F. Thomsen, and J. T. Gosling. Ions upstream of the earth's bow shock: A theoretical comparison of alternative source populations. *J. Geophys. Res.*, 88(A3):2039–2047, Mar. 1983. doi: 10.1029/JA088iA03p02039.
- S. J. Schwartz, C. J. Owen, and D. Burgess. *Astrophysical Plasmas*. University of London, 2004. URL <http://www.sp.ph.ic.ac.uk/~sjs/APmaster.pdf>.
- S. J. Schwartz, E. Henley, J. Mitchell, and V. Krasnoselskikh. Electron Temperature Gradient Scale at Collisionless Shocks. *Phys. Rev. Lett.*, 107(21):215002, Nov. 2011. doi: 10.1103/PhysRevLett.107.215002.
- N. Sckopke, G. Paschmann, S. J. Bame, J. T. Gosling, and C. T. Russell. Evolution of ion distributions across the nearly perpendicular bow shock: specularly and non-specularly reflected-gyrating ions. *J. Geophys. Res.*, 88(A8):6121–6136, Aug. 1983. doi: 10.1029/JA088iA08p06121.
- C. P. Sonett and I. J. Abrams. The Distant Geomagnetic Field, 3, Disorder and Shocks in the Magnetopause. *J. Geophys. Res.*, 68(5):1233–1263, Mar. 1963. doi: 10.1029/JZ068i005p01233.
- M. Svensson. Electron heating in collisionless shocks observed by the mms spacecraft. Master's thesis, Luleå University of Technology, Space Technology, 2018.
- D. G. Swanson. *Plasma waves*. Institute of Physics Publishing, 1989. ISBN 0 7503 0927 X.
- M. F. Thomsen. Upstream suprathermal ions. *Washington DC American Geophysical Union Geophysical Monograph Series*, 35:253–270, Jan. 1985. doi: 10.1029/GM035p0253.
- L. Turc, U. Ganse, Y. Pfau-Kempf, S. Hoilijoki, M. Battarbee, L. Juusola, R. Jarvinen, T. Brito, M. Grandin, and M. Palmroth. Foreshock properties at typical and enhanced interplanetary magnetic field strengths: Results from hybrid-vlasov simulations. *Journal of Geophysical Research: Space Physics*, 123(7): 5476–5493, 2018. doi: <https://doi.org/10.1029/2018JA025466>. URL <https://agupubs.onlinelibrary.wiley.com/doi/abs/10.1029/2018JA025466>.
- A. A. Vlasov. *Many-particle theory and its application to plasma*. Gordon & Breach Science Publishers, 1961. ISBN 0677203306.

- S. von Alfthan, D. Pokhotelov, Y. Kempf, S. Hoilijoki, I. Honkonen, A. Sandroos, and M. Palmroth. Vlasiator: First global hybrid-Vlasov simulations of Earth's foreshock and magnetosheath. *Journal of Atmospheric and Solar-Terrestrial Physics*, 120:24–35, Dec. 2014. doi: 10.1016/j.jastp.2014.08.012.
- S. N. Walker, H. S. C. K. Alleyne, M. A. Balikhin, M. André, and T. S. Horbury. Electric field scales at quasi-perpendicular shocks. *Annales Geophysicae*, 22(7):2291–2300, 2004. doi: 10.5194/angeo-22-2291-2004. URL <https://angeo.copernicus.org/articles/22/2291/2004/>.
- D. Winske and K. B. Quest. Magnetic field and density fluctuations at perpendicular supercritical collisionless shocks. *J. Geophys. Res.*, 93(A9):9681–9693, Sept. 1988. doi: 10.1029/JA093iA09p09681.
- Z. Yang, Y. D. Liu, G. K. Parks, P. Wu, C. Huang, R. Shi, R. Wang, and H. Hu. Full Particle Electromagnetic Simulations of Entropy Generation across a Collisionless Shock. *Astrophysical Journal Letters*, 793(1):L11, Sept. 2014. doi: 10.1088/2041-8205/793/1/L11.